Identification of interaction mechanisms during drag finishing by means of an original macroscopic numerical model

Irati Malkorra, Hanène Souli, Christophe Claudin, Ferdinando Salvatore, Aude Mathis, Pedro Arrazola, Joël Rech, Jason Rolet, Herve Seux

Title page

Identification of interaction mechanisms during drag finishing by means of an original macroscopic numerical model

Irati Malkorra[*a,b]: irati.malkorra@irt-m2p.fr

Hanène Souli[b]: hanene.souli@enise.fr

Christophe Claudin[b]: christophe.claudin@enise.fr

Ferdinando Salvatore[b]: ferdinando.salvatore@enise.fr

Pedro Arrazola[c]: pjarrazola@mondragon.edu

Joel Rech[b]: joel.rech@enise.fr

Hervé Seux[b]: herve.seux@enise.fr

Aude Mathis[d]: aude.mathis@naval-group.com

Jason Rolet[a]: Jason.rolet@irt-m2p.fr

[a]IRT-M2P, 4 Rue Augustin Fresnel, 57070 Metz, France

[b] University of Lyon, Ecole Centrale de Lyon - ENISE, LTDS CNRS UMR 5513, 58 Rue Jean Parot, 42000 Saint-Etienne, France

[c]Faculty of Engineering, Loramendi 4, Mondragon University, 2500 Arrasate, Spain

[d]Naval Group, CESMAN, Technocampus Ocean, 5 rue de l'Halbrane, 44340 Bouguenais, France

* Corresponding author. *E-mail address:* irati.malkorra@irt-m2p.fr

Abstract

Drag finishing is one of the mass finishing processes that enhances surface roughness on complex parts due to the mechanical action of abrasive media. Due to the complexity of the process, industrial practice is based on experience. This paper proposes a model simulating abrasive media flowing around a part during a drag finishing operation at a macroscopic scale. The 2D model is based on an Arbitrary Lagrangian Eulerian (ALE) formulation that provides relevant mechanical parameters such as the distribution of stresses (normal and shear stresses) and sliding velocities between abrasive media and the surface to be polished. Abrasive media are modelled as a continuous material with a Drucker-Prager plastic constitutive equation. This last has been calibrated as a result of triaxial testing, commonly used to characterise soils in civil engineering. Two abrasive media (spherical and pyramidal shape) having the same composition were characterised. Pyramidal media exhibit significantly higher rheological behaviour compared to spherical one. The model is shown to be very sensitive to the media's rheological behaviour but also to the immersion depth. Pyramidal media leads to much higher normal and shear stresses, which are even higher at deeper immersion depths. Drag finishing experimental tests were carried out to evaluate the efficiency of the model. The correlation between experimental drag finishing tests and numerical test results reveals the physical mechanisms at the interface between media and the surface. Spherical media, with a small/orthogonal orientation impact angle, promotes plastic deformation, while the main mechanisms becomes cutting at higher impact angles. However, pyramidal media promotes cutting irrespective of the orientation angle. Moreover, it was concluded that the optimal mechanical loading combination happens between 30 and 60° for both medias, as the shearing energy reaches its maximum value.

Keywords: Drag finishing; Numerical modelling; Arbitrary Lagrangian Eulerian (ALE) formulation; Abrasive media shape; Rheological behavior; Abrasive wear.

Nomenclature

h	Immersion depth of the workpiece [m]
ω_1	Drag velocity of the workpiece [rpm]
v	Sliding velocity of media [m/s]
σ_n	Normal stress [Pa]
τ	Shear stress [Pa]
α	Surface orientation regarding the media flow [°]
ρ_{bulk}	Media bulk density [kg/m³]
α_m	Media impact orientation [°]
F	Contact force [N]
Sa	Surface roughness [µm]
δ	Workpiece height [mm]
p	Hydrostatic pressure [Pa]
r	Radius of the workpiece [m]
v_{linear}	Linear velocity [m/s]
A	Area of the container in the x-z plane [m²]
g	Gravity [m/s²]
μ	Friction coefficient [-]
E	Young's Modulus [Pa]
ν	Poisson's ratio [-]
φ	Friction angle [°]
ψ	Dilatancy angle [°]
K	Ratio between the yield stress in triaxial tension to triaxial compression [-]

q	First invariant of stress [Pa]
p	Von Mises equivalent stress [Pa]
S_{ij}	The deviatoric stress [Pa]
f	Yield function
c	Cohesion [-]
r	Third stress invariant [Pa]
G	Flow potential [Pa]
σ_3	Confining pressure [Pa]
σ_1	Vertical pressure [Pa]
ε_y	Vertical strain [%]
ε_v	Volumetric strain [%]
e_{min}	Minimum void ratio [-]
e_{max}	Maximum void ratio [-]
D_r	Relative density [%]
e	Void ratio [-]
ρ_{grain}	Abrasive media grain density [kg/m^3]
m_{sec}	Mass of the media [kg]
Cu	Coefficient of uniformity [-]
d_{sample}	Diameter of the sample [m] (triaxial tests)
h_{sample}	Height of the sample [m] (triaxial tests)
q_{triax}	Deviatoric stress [Pa]
p'	Effective mean stress [Pa]
M	Slope of the yield limit in the plane q_{triax}- p' [°]
$F_{y\ macro\ exp.}$	Experimental drag force [N]
$F_{y\ macro\ num.}$	Numerical drag force [N]
A_{peak}	Peak area [µm^2]
A_{valley}	Valley area [µm^2]

1 Introduction

Drag finishing is a mass finishing technique that improves the surface roughness of external surfaces of parts. Parts are clamped on a spindle and submerged into a mixture of abrasive media and liquid compound (Figure 1a), then a motion is applied to the part [1]. It belongs to the family of abrasive fine-finishing processes with other well-known processes such as vibratory finishing, barrel finishing, etc. Drag finishing is prioritised, to finely finish components such as medical implants and turbine blades, with the objective of preventing any contact between parts [2]. This process has received limited attention compared to other finishing processes, as it is often used to produce small batches. The optimisation of the process is based on the empirical knowledge of the company. However, its application becomes even more popular with the development of 3D printed parts that requires post-processing using finishing operations; some researchers employed vibratory finishing [3–6], whereas others also tested the drag finishing and the stream finishing process [7]. In the case of this last system, the rotational motion is given to the bowl rather than to the part [1]. The complexity and the high added value of the new generation of components make it necessary to have a scientific understanding of drag finishing.

Most of the scientific papers that investigated drag finishing, have conducted experimental investigations with the aim of evaluating the sensitivity to technological parameters such as drag velocity, shape and size of abrasive media, composition of the liquid compound, process duration, etc. For instance, Kacaras et al. [8], Barletta et al. [9] and Zanger et al. [10] showed that a higher rotational speed facilitates the reduction of surface roughness. Uhlmann et al. [11] verified that pyramidal media (containing sharp edges) are more

prone to scratch the roughness peaks, whereas spherical media deform it plastically. Malkorra et al. [12] investigated the size of the media and confirmed that large media are more prone to reduce surface roughness, which seems to be correlated to the impact forces, as suggested by Song et al. [13]. The composition of the liquid compound, spread in drag finishing, influences the surface finish through a modification of the mechano-chemical mechanisms. The liquid is responsible for evacuating the debris from the machine [14,15], as well as for inducing a gentle chemical action that accelerates the efficiency of the process [13]. Based on a large number of experiments, some authors proposed phenomenological models (surface response) to predict the surface roughness. For instance, as far as vibratory finishing is concerned, Domblesky et al. [16] proposed a phenomenological model depending on bowl acceleration, media weights, specific energy and a cutting factor, taking into account the efficiency of a defined abrasive medium. These works make important contributions to a better understanding of the process for a defined application. However, they do not enable the prediction of the best working conditions for any other application or working conditions. With the development of 3D printed parts that are customized individually, drag finishing conditions have to be adapted. Considering the cost of such components, there is a high need to develop models to predict the evolution of surface roughness over the part during drag finishing.

Drag finishing is a multiscale process as shown in Figure 1. The development of a predictive model requires to address the relevant scale. At a macroscopic scale, drag finishing can be considered as a part moving through a homogeneous material having the mechanical properties of an abrasive slurry (Figure 1,a). At a mesoscopic scale, the slurry can be considered as a mixture of some abrasive media within a liquid compound (Figure 1,b)). Finally, at a microscopic scale (Figure 1,c)), drag finishing can be considered as a single abrasive media (a particle) interacting with the surface having a complex surface topography (surface roughness). There is a clear link between the three scales of modelling. It is obvious that the macroscopic movement influences the local orientation and the contact of the media, at the mesoscopic scale, and the scratching phenomena, at a microscopic scale. However, in the current state of the art, no comprehensive model is able to simultaneously describe all of the mechanisms that happen at all scales This means that none of the models explain the link between macroscopic, mesoscopic and microscopic phenomena. It is only possible to find some models at a single scale.

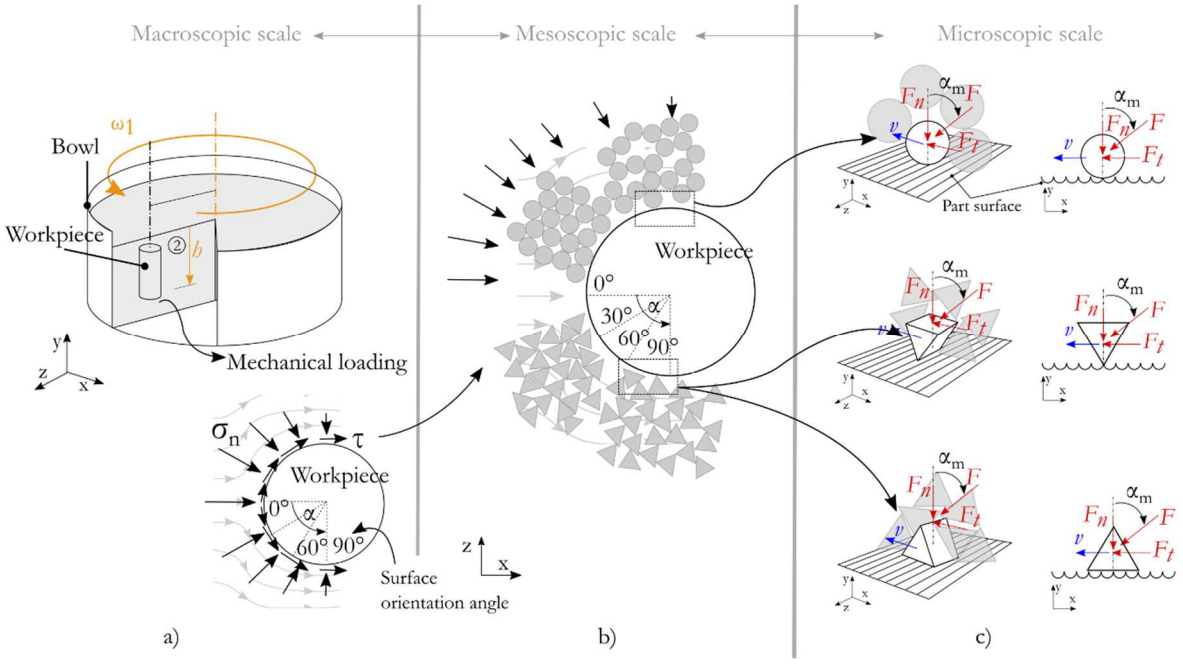

Figure 1. ***Drag finishing, a multiscale process.*** *Drag finishing process at a) a macroscopic scale considering media as an abrasive slurry and the resultant mechanical loadings (normal and shear stresses, σ_n et τ) at the interface. b) At a mesoscopic scale, where the mixture of abrasive media (discrete particles) interacts with the part to polish. c) Finally, at a microscopic scale single abrasive particles interacts with the surface roughness under different contact forces (F_n, F_t, F), sliding velocities (v) and orientation angles (α_m).*

the slurry can be considered as a mixture of some abrasive media within a liquid compound

At a macroscopic scale, drag finishing can be considered as a part moving through a homogeneous material with the mechanical properties of an abrasive slurry. The part can be modelled as a rigid volume but the surface roughness cannot be considered at this scale. The mechanical loading applied by the abrasive slurry around the part depends on its composition and rheological properties. It also depends on the immersion depth of the part (*h*) and on the drag velocity (ω_1) (Figure 1a). At this macroscopic scale, drag finishing can be modelled as a non-Newtonian fluid flowing around the part. Such a model can provide the physical parameters such as the velocity (v), the normal stress (σ_n) and shear stress (τ) inside the abrasive slurry and around the part (Figure 1a). This may contribute to a better understanding of the process, such as the variation of the stresses (σ_n and τ), with regard to the orientation of the surface (α) (Figure 1a). For instance, it may enable quantification of the normal stress (σ_n) applied on a surface oriented perpendicular to the flow (α=0° in Figure 1a), which should be higher than the normal stresses (σ_n) applied on a surface oriented parallel to the flow (α=90° in Figure 1a). It is not possible to make a direct prediction of surface roughness (microscopic scale) from physical parameters (σ_n, τ and v) at a macroscopic scale but it is possible to make a statistical correlation between them based on experimental observations. On the contrary, by integrating a physical equation that takes into account local, macroscopic parameters, such as σ_n, τ and v, a model at a macroscopic scale may have the potential to predict the evolution of a part's macroscopic geometry (dimension, geometry) as proposed by Rech et al. [17] in a different application, i.e. cutting. Similar approaches were proposed by Dražumerič et al. for grinding [18].

At this macroscopic scale, very few researchers in drag finishing (or tribofinishing in general) have modelled the slurry as a homogeneous material. Such approaches are more common in civil and chemical engineering. Three types of numerical formulations are employed: CFD (Computational Fluid Dynamics) [19,20], Eulerian [21] and Finite Element formulations [22]. Some of these treated the granular material as a fluid-like material [19,20], whereas others threated it like a solid [21,22]. These models were created to study the motion of granular media under different conditions. However, none of them proposed a model to analyse the interaction between granular media (in motion) with another component. In chemical engineering and in civil engineering, scientists are interested in the movement of the granular material embedded in a container and not in the interaction with a part located in the heart of the media, as in drag finishing. In tribofinishing processes, the key issue is to model the interaction between granular media and the workpiece to be polished. So, there is a clear need to develop a more advanced model considering the interaction between media and a workpiece at a macroscopic scale, applied to drag finishing purposes.

In addition to the previous statement, it is necessary to underline that the formulations presented in the literature [22] consider two types of constitutive equations to describe the rheological behaviour of the material. Some constitutive equations are based on the kinetic theory of liquids [19,20] which are more suitable for low density materials submitted to rapid deformations. These models are common in chemical engineering. The second types of constitutive equations are the ones employed in soil mechanics, such as the Mohr-Coulomb and Drucker-Prager models, based on plasticity theory. This last is considered to be one of the most adequate methods for dense granular materials with slow deformations [23]. Unfortunately, the identification of a constitutive model's parameters remains an issue. Some authors, such as Zheng and Yu [21], employed a Mohr-Coulomb elastoplastic model, but they do not explain their method for identifying model parameters. Other authors prefer to identify the parameters by indirect methods. For example, Cariapa et al. [20] employed a Granular Surface Fitting method (GSF), based on a trial-and-error approach. A CFD model is calculated with a kinetic viscosity, then the slope of the media free surface is compared to the experimental one. Various kinetic viscosities were tested until the one that best fits the experimental results was found. In the case of Hashemnia and Spelt [22], they identified the friction angle of the material for the Drucker Prager plasticity model by an additional DEM (Discrete Element Method, to be described in this section) model of a tub finisher to measure shear rate and the stress tensor in different points of the model. These indirect approaches are not satisfactory from a

scientific point of view. It is a basic way to work around the problem. There is a clear need to identify constitutive equations of abrasive media by direct methods. Such approaches exist in civil engineering [24,25] but, to date, none of these methods have been applied to characterise abrasive media. This is a free field for research.

At a mesoscopic scale, the slurry can be considered as a mixture of some abrasive media within a liquid compound (Figure 1b). At this scale, the slurry may be modelled as discrete solid particles interacting together during their movement. The bulk density (ρ_{bulk}) of the group of media within an elementary volume depends on the local pressure and on the velocity during the movement. For instance, it is clear that the bulk density (ρ_{bulk}) of media should be higher in front of the part (high pressure at α=0° in Figure 1a), whereas it should be lower in the lateral area (low pressure at α=90° in Figure 1a). Inside an elementary volume, the orientation of the media (α_m) (Figure 1,c), the number of contacts between the media, and the intensity of the contact forces (F) between the media also depend on the normal stress (σ_n) and on the velocity (v), considered at the macroscopic scale. At the interface between the slurry and the part, the orientation of the media (α_m), the number of contacts between the media and the surface, and the intensity of the contact forces (F) between the media and the surface depends on the normal stress (σ_n) and on the local sliding velocity (v). As suggested by Figure 1b, the situation should be very different for media composed of spherical particles or pyramidal particles due to the interlocking effect between pyramidal media. The surface of the part can only be modelled by a simple geometry (plane, cylinders, etc.) and the surface roughness cannot be considered at this scale. So, at this mesoscopic scale, models cannot predict the evolution of surface roughness (microscopic scale) from the physical parameters obtained at a mesoscopic scale. Such mesoscopic models may only predict the movement and the mechanical interactions between a certain number of media and a simple surface. By considering a physical equation (i.e. wear equation) taking into account a statistical distribution of contact forces and velocity between media and the surface, these models may have the potential to predict the evolution of the local mesoscopic geometry (flatness, circularity, etc.).

At the mesoscopic scale, researchers proposed DEM-based models (Discrete Element Method) where the abrasive particles (discrete elements) interact with the parts to polish. The major limitation of DEM models is the computational time, as well as the difficulty of modelling complex shaped media, such as pyramids. Some authors proposed the assembly of discrete spherical elements, to build complex geometric grains [26][27] but the majority of research work considered spherical media. Naeini and Spelt [28] studied the abrasive media motion and velocities in a rotating drum. Uhlmann et al. [29] modelled the interaction of a high number of abrasive particles with the part to be polished by drag finishing. They focused on predicting contact forces (F), with the aim of predicting the material removal [30]. Salvatore et al. [31] proposed a similar DEM model. On the contrary, Makiuchi et al. [32] proposed the most advanced model for predicting the material removal due to the contact forces (F) and the velocities (v) provided by a DEM model in vibratory finishing. They selected Preston's Law [33] to predict the evolution of the local mesoscopic geometry. Finally, Zanger et al. [10] proposed a DEM model of the stream finishing process and they correlated the distribution of the normal force (F) and the sliding velocity (v) of the particles around the part, with experimentally measured material removal.

Finally, **at a microscopic scale** (Figure 1c), drag finishing can be considered as a single abrasive media (particle) interacting with the surface having a complex surface topography (surface roughness). Depending on the interactions between the surrounding media, the orientation of the considered particle (α_m), the contact force (F) and its velocity (v), a medium will induce various interaction mechanisms (plastic deformation, ploughing or scratching) as described by Kato et al. [34]. These interaction mechanisms depend on the effective contact between the particle and the peaks of the surface topography. As suggested in Figure 1c, the orientation of a pyramidal particle will affect the nature of the contact, whereas a spherical particle leads to a more deterministic contact. By considering a physical equation (wear equation), taking into account a statistical distribution of particle orientation with a range

of contact forces (*F*), velocities (v), and trajectories, these models may predict the evolution of surface roughness (*Sa*).

At a microscopic scale, a large number of investigations have been conducted among the specialists in tribology. Most of this research focused on investigating the physics of either cutting mechanisms (chip formation), plastic deformation or ploughing, as in the case of Avient et al. [35], Samuels [36], Kato [37] and Hashimoto [38]. They analysed the abrasion of metals with single grains by studying the grooves from scratch tests under various contact conditions, attack angles and degrees of penetration. More recently, Dražumerič et al. [18] published the theory of aggressiveness, an analytical model that takes into account the geometrical aspects and kinematics in an abrasive contact. However, researchers like Hilero and Mathia [39], Domblesky et al. [16], Hashimoto et al. [38] and Li et al. [26] created more advanced models of tribofinishing processes, as functions of process velocity or bowl acceleration, the media-part's number of contacts, the specific energies and the cutting factor of each type of abrasive media.

The present paper is focused on modelling drag finishing at a macroscopic scale. **The first objective** consists of proposing a model that simulates the flow of abrasive media (considered as a homogeneous and continuous material around a workpiece), as well as its interaction with this workpiece. This is a new numerical model of drag finishing based on an ALE formulation. The model permits calculation of the mechanical loadings (velocity (v), normal stress (σ_n) and shear stresses (τ)) induced around the part.

The second objective of this paper is to bring a contribution to the characterisation of the macroscopic, rheological properties of abrasive media. The literature review has revealed a weakness as only indirect methods were proposed to characterise the rheological properties of abrasive media. In this paper, a direct method is proposed: the triaxial test, which is used in the field of soil mechanics. The Drucker Prager plasticity model is identified.

As the development of a numerical model requires experimental validation, an original experimental set-up has been proposed. It enables measurement of the macroscopic drag force applied on the part. This physical parameter is then compared to its numerical estimation.

The ALE model, the identification of the rheological model and the experimental validation are applied, to investigate the drag finishing process of a cylindrical part made of AISI1045 steel with two kinds of abrasive media (spherical and pyramidal).

Experimental drag finishing tests were performed. The evolution of surface roughness around the part is investigated over time. **The third objective** of the paper proposes a correlation between the physical parameters (velocity (v), normal stress (σ_n) and shear stress (τ)) at a macroscopic scale and the evolution of surface roughness (microscopic scale) around the workpiece so as to reach a better understanding of the mechanisms (plastic deformation or abrasion) controlling the efficiency of the drag finishing process.

2 Description of the numerical model

The proposed model aims to simulate the flow of abrasive media at a macroscopic scale. The geometrical and kinematic parameters of the model are based on the drag finishing set-up proposed by Malkorra et al. [12] (Figure 2a). A cylindrical workpiece rotates around the y-axis of the bowl with a speed of ω_1=60 rpm. This kinematic differs from traditional drag finishing as the workpiece does not rotate around its own axis. So, the abrasive media always faces the same surface. As the workpiece has a large height (δ) (80 mm), the media is supposed to flow on each side of the cylinder (plane X-Z) and not in the vertical direction Y (Figure 2a and 2b). The configuration can be simplified by multiple 2D plain strain models (Figure 2c) at various immersion depths (*h*). For one section (X-Z), at an immersion depth (*h*), the corresponding model has to take into account the hydrostatic pressure (*p*) at this level. The dimensions of the container were Ø 650 mm x 400 mm.

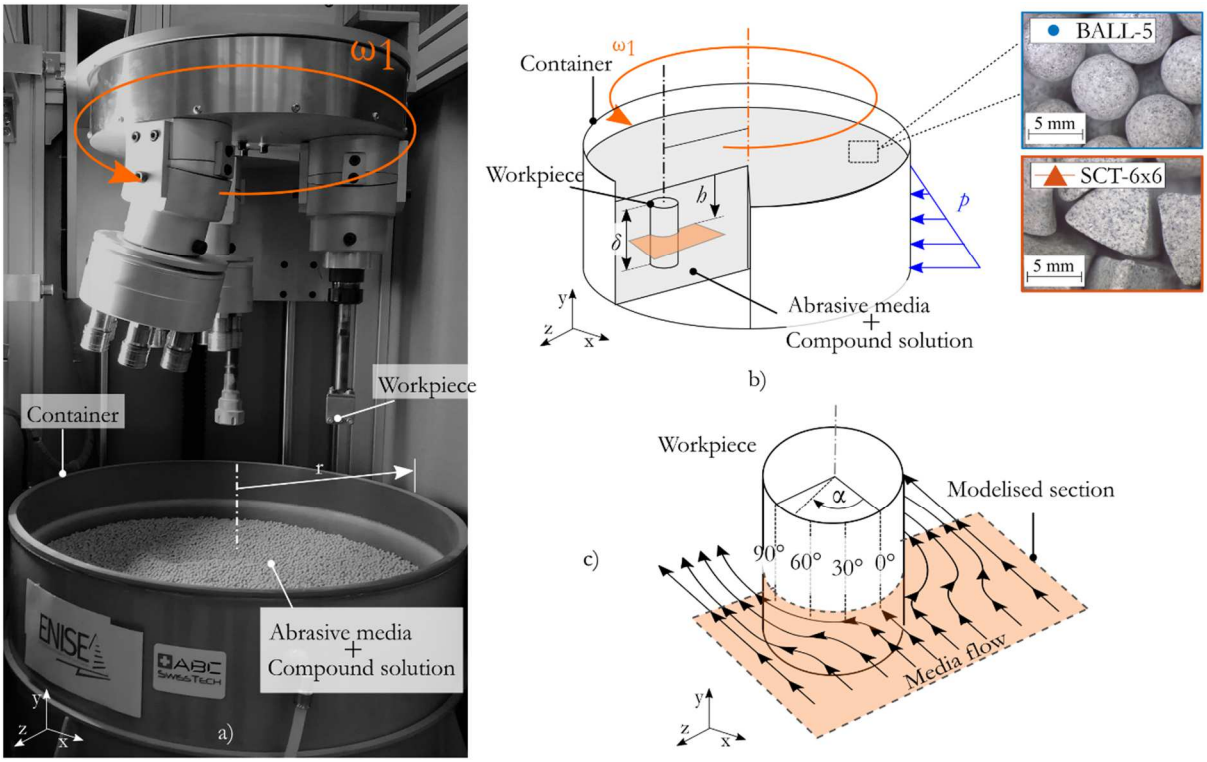

Figure 2. ***The experimental set-up.*** *a) The drag finishing machine and the motion applied to the system (ω_1), b) the schematic drawing of the set-up indicating the rotational speed (ω_1), the immersion depth (h), the height of the part (δ) and the hydrostatic pressure (p). And in c) the interaction between the part and media flow. The analysed orientation angles (α) (0, 30, 60, 90°) were indicated in c) as well as the modelled section.*

The model was developed with the commercial code Abaqus/Explicit© and divided into two parts (Figure 3). The 'workpiece' consisted of a Lagrangian rigid circle with a radius of r=0.01 m (the grey circle in Figure 3). Its movement was constrained in all directions in its axis. The 'media' was defined as a deformable homogeneous material and an ALE formulation was employed to permit the flow of the material inside the mesh (from the left to the right side). The inflow and outflow surfaces for the material were defined as Eulerian Surfaces (ES) and the flow direction was plotted (the black arrows in Figure 3). A speed of v_{linear}=1 m/s was applied to the media in the inflow surface. The surfaces, where material flow was not allowed, are defined as Lagrangian Surfaces (LS). A static pressure *p* was applied in the inflow and outflow surfaces (blue arrows in Figure 3). Its value was estimated by Eq. 1, where ρ_{bulk} is the bulk density of the granular material, *A* is the area of the container in the x-z plane (Figure 2), *h* is the immersion depth (m) and *g* is gravity.

$$p = \rho_{bulk} \cdot A \cdot h \cdot g \qquad \textit{Eq. 1}$$

Both parts were meshed with 4 node plane strain elements (called CPE4R) with a uniform distribution. The approximate size was 0.98 mm. A sensitivity study was carried out to define the optimal size of the elements. Smaller elements were tested but those did not provide more precise numerical results, besides, the numerical calculation was more time consuming. The contact interaction between the flow of the media and the workpiece is defined by a kinematic contact algorithm, with a finite sliding formulation and a Coulomb friction coefficient (μ) of 0.25 [40].

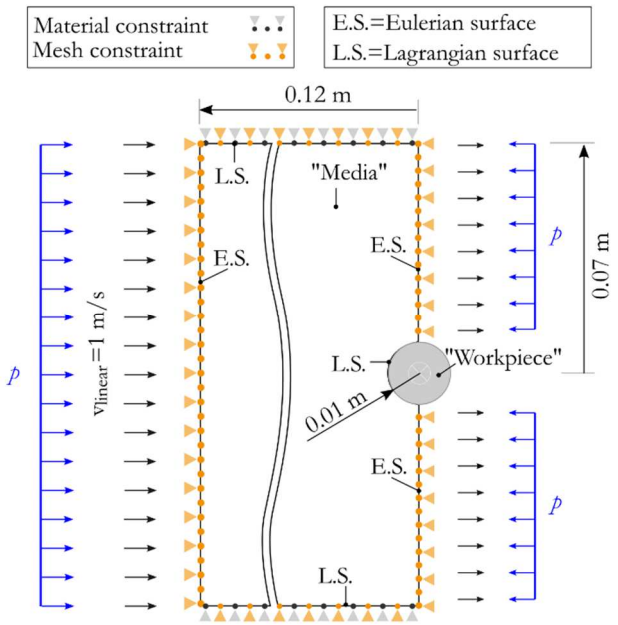

Figure 3. ***The numerical model.*** *The schematic description and dimensions of the model composed by two parts: the media and the workpiece. Material and mesh constraints are indicated, as well as the Eulerian and Lagrangian surfaces. The applied mechanical loads are also shown, the hydrostatic pressure (p) and the velocity of the material (v_{linear}).*

The media belong to the family of granular materials. Such materials have been deeply investigated in civil engineering, especially to characterise the mechanical behaviour of soils. They can be modelled as homogeneous and continuous materials at a macroscopic scale. The mechanical properties to define the elasto-plastic behaviour of the granular material (the group of abrasive media) are: the bulk density (ρ_{bulk}), the elastic properties [Young's modulus (E), Poisson's ratio (ν)] and plastic properties [the friction angle (φ), the dilatancy angle (ψ), and the ratio between the yield stress in triaxial tension to triaxial compression (K)].

The Young's Modulus, (E) of granular materials is much lower than those of metals, between 200 kPa and 1 MPa [21,22]. Whereas the Poisson's ratio varies between 0.20 and 0.35, according to Braja et al. [41]. The stress-strain relation is described by a Drucker Prager (D-P) linear criterion [42], as it is commonly used for soils or granular materials [22,43].

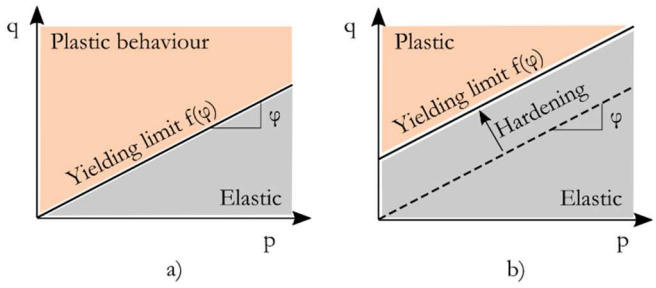

Figure 4. ***Schematic description of the Drucker Prager linear criterion.*** *a) the yield surface in the meridional plane (q-p), and b) new yield surface after the hardening. The yielding limit (between materials elastic and plastic behaviour) is defined by the friction angle (φ) of the material.*

In Figure 4a, the yield surface is represented in the meridional plane q-p. These are the stress invariants: p is the first invariant of stress representing the equivalent pressure and it is expressed by Eq. 2. Whereas q is the von Mises equivalent stress, defined by Eq. 3, where S_{ij} is the deviatoric stress, defined by Eq. 4.

$$p = -\frac{1}{3} trace(\sigma_{ij}) \qquad \text{Eq. 2}$$

$$q = \sqrt{\frac{3}{2} S_{ij} S_{ij}} \quad \text{Eq. 3}$$

$$S_{ij} = \sigma_{ij} - \frac{1}{3}\sigma_{ij}\delta_{ij} \quad \text{Eq. 4}$$

The yield surface is the border between the elastic and plastic behaviour of the material. The yield function *f* defines this border using Eq. 5, where *t* is defined by Eq. 6 and explained in the next paragraph. p is the equivalent stress, φ the friction angle and *c* the cohesion of the material.

$$f = t - p\tan\varphi - c = 0 \quad \text{Eq. 5}$$

Unlike the case of metal materials, the strength of granular materials is asymmetrical between tension and compression. For example, the strength in compression is higher than in tension. The ratio (*K*) between the yield stress in triaxial tension and the yield stress in triaxial compression is employed to describe this asymmetry. This parameter defines the term *t* (expressed in Eq. 6), where q is the equivalent von Mises stress and *r* the third stress invariant. Because of the term *t* in the Drucker Prager yield function (in Eq. 5), it is possible to match different yield values if the material is in compression or tension. The ratio *K* takes values between $0.778 \leq K < 1$.

$$t = \frac{1}{2} q \left[1 + \frac{1}{K} - \left(1 - \frac{1}{K}\right)\left(\frac{r}{q}\right)^3\right] \quad \text{Eq. 6}$$

The friction angle (φ) is the slope of the yield surface. This parameter is the sum of the local friction between surfaces (μ) and the interlocking between the particles, and its value varies between 30 and 40° in granular materials [41]. Concerning the cohesion *c* in the case of abrasive media, it is considered as zero (c=0), as stated by [21].

Once the material reaches the yielding limit, hardening of the material occurs (see Figure 4b). In the model, the hardening was defined in uniaxial compression and the flow potential (*G*) applied was expressed, as in Eq. 7, where ψ is the dilatancy angle of the material. This parameter describes how the material dilates or contracts under a force. Its value is always lower than the internal friction angle. Since Dano et al. [44,45], it is 30° lower.

$$G = t - p\tan\psi \quad \text{Eq. 7}$$

The parameters mentioned are necessary to define the mechanical behaviour of the material. In this paper, the ratio (*K*) has been kept constant (*K*=0.8), because of the work of [46]. The rest of the parameters [bulk density (ρ_{bulk}), Young's Modulus (E), Poisson's ratio (ν), friction angle (φ), and dilatancy angle (ψ)] have to be determined by the methods used in soil mechanics [25]. The procedure and the results will be detailed in section 3.

3 Characterisation of the rheological properties of the granular material

Some of the parameters required to define the rheological behaviour of the granular material, such as Young's Modulus (*E*), Poisson's ratio (ν), friction angle (φ) and dilatancy angle (ψ), have been identified by means of a triaxial compression test. This technique is commonly used to characterise the mechanical properties of geomaterials. This characterisation method has been applied for two abrasive media: a spherical (5 mm in diameter) and a pyramidal (6x6 mm) media, as shown in Figure 8.

3.1 Principle of triaxial compression tests

The basic idea behind triaxial compression tests consists of embedding a certain amount of media within a deformable cylinder (called a membrane, see Figure 5c) and applying a variable confining pressure (σ_3) on it (Figure 5a and 5b). During the application of the pressure, the deformation is observed (ε_y, ε_v). By making a link between stress and strain, some mechanical properties can be identified. The present work

has been performed on a triaxial set-up from the company *Sols Mesures*. Samples were prepared in a deformable membrane, made of rubber (provided by *PiercanTech)*, and having the following dimensions (Figure 5c): Ø=100 mm, l=300 mm and thickness=0.5 mm.

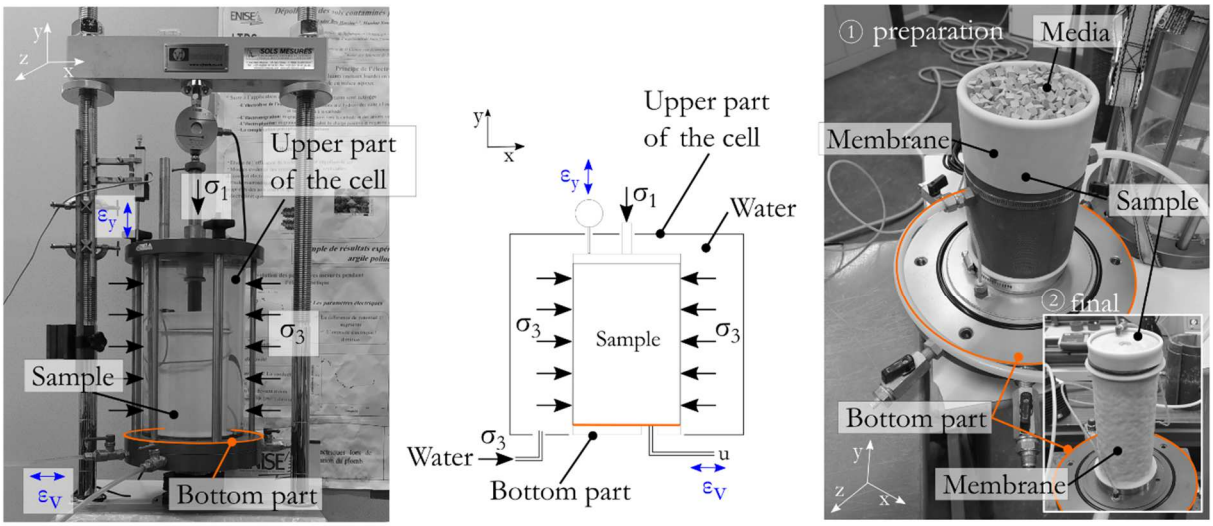

Figure 5. ***The triaxial tests for media characterisation.*** *a) The employed triaxial cell and its b) schematic illustration where the sample, the applied stresses (σ_1,σ_3) and the deformation sensors (ε_y, ε_v) are shown. In c), sample preparation is shown: 1) abrasive media embedded in the deformable membrane and 2) the closed sample is also shown.*

3.1.1 Sample preparation

Samples of two abrasive media were prepared: spherical media (BALL-5 mm) and a pyramidal media (SCT-6x6 mm), made of vitrified aluminium oxide grits embedded in a ceramic bonder. All samples were prepared as explained bellow.

The preparation of the samples is crucial in order to have the same bulk density (ρ_{bulk}) in all samples. It is known that each granular material can have different compaction levels. Youd [47] defined the minimum and maximum void ratios (e_{min} and e_{max}) that a granular material could have, depending on the shape of the grains. The compaction of the abrasive media during drag finishing is not very high; the drag movement of the workpiece dilates the media but the hydrostatic pressure applied by the media, located above, compacts them again. So, it is considered that the degree of compaction (e) must be between the maximum and the minimum void ratios of the material, as illustrated in Figure 6.

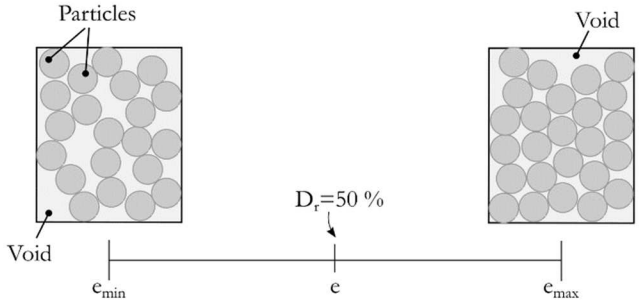

Figure 6. The various compaction levels of granular materials, maximum and minimum void ratios (e_{min} and e_{max}) and the void ratio (e) for a relative density D_r of 50%.

The degree of compaction is defined by the relative density (D_r) using Eq. 8, where e_{max} and e_{min} are the maximum and the minimum void ratios that the granular material can adopt, and e is the void ratio of the sample for a certain relative density D_r.

$$D_r = \frac{e_{max} - e}{e_{max} - e_{min}} \quad \text{Eq. 8}$$

The maximum and minimum void ratios (e_{max}, e_{min}) are extracted from the Youd tables [47]. For a Dr = 50%, and assuming that all particles are identical (Cu=1), the void ratio (e) of the sample was calculated.

The void ratio (e) links the bulk density (ρ_{bulk}) and the individual grain density (ρ_{grain}) in Eq. 9. The grain density was measured with a pycnometer (ρ_{grain}=2.46 g/cm^3) and the bulk density (ρ_{bulk}) of the sample was calculated.

$$e = \frac{\rho_{grain}}{\rho_{bulk}} - 1 \quad \text{Eq. 9}$$

Finally, the mass of the material (m_{sec}) required in the sample to reach a relative density (D_r) of 50%, was deduced by Eq. 10, where d_{sample} is the diameter and h_{sample} is the height of the sample.

$$\rho_d = \frac{m_{sec}}{V_T} = \frac{m_{sec}}{\pi \cdot \frac{d^2}{4} \cdot h} \quad \text{Eq. 10}$$

Table 1 shows the physical properties for both media studied in this work, as well as the mass (m_{sec}) of the sample.

Table 1. The physical properties and the total mass of the media in the samples for both spherical and pyramidal abrasive media.

Media	Shape	Cu [-]	e_{max} [-]	e_{min} [-]	ρ_{grain} [kg/m^3]	ρ_{bulk} [kg/m^3]	m_{sec} [gr]
Spherical (BALL-5)	Sub-Rounded	1	0.9	0.5	2460	1510	2312
Pyramidal (SCT 6x6)	Sub-Angular	1	1	0.6	2460	1770	2448

NB: ≈2 kg of media were used to fill the membrane. Moreover, 30 mL of water was added so as to humidify the media in the same way as in the drag finishing machine (0.015 kg of water for 1 kg of media).

3.1.2 Testing procedure

Samples (abrasive media embedded in the deformable membrane) were placed in the triaxial cell, see Figure 5a and 5b. The sample was surrounded by water (Figure 5a and 5b) so as to apply a confining pressure (σ_3), which remained constant during the test. Afterwards, a vertical pressure (σ_1) was progressively applied to deform the sample, until 20% of vertical strain (ε_y) (in the vertical direction of the sample in Figure 5). The speed of deformation was fixed at 0.02 mm/min. During the application of the vertical pressure (σ_1), the deviatoric stress (q_{triax}) (Eq. 11), the effective mean stress (p') (Eq. 12), the vertical strain (ε_y) and the volumetric strain (ε_v) were measured (Figure 5a and 5b). It was mandatory to apply at least 3 levels of confining pressure (σ_3) so as to identify the mechanical properties. In the present work, the confining pressure (σ_3) was set at 20, 40 and 80 kPa.

$$q_{triax} = \sigma_1 - \sigma_3 \quad \text{Eq. 11}$$

$$p' = \frac{\sigma_3 - (\sigma_1 - \sigma_3)}{3} \quad \text{Eq. 12}$$

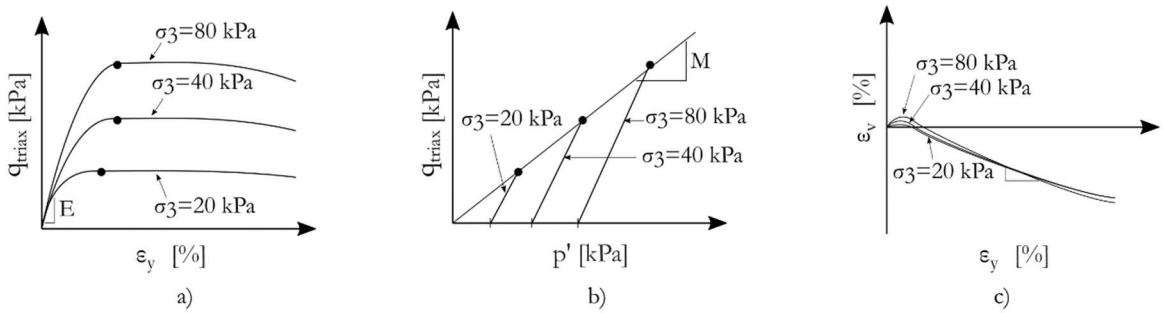

Figure 7. ***The typical representation of triaxial test results:*** *a) deviatoric stress (q_{triax}) vs. the vertical strain (ε_y), b) deviatoric stress (q_{triax}) vs. the effective mean stress (p') and c) radial strain (ε_v) vs. vertical strain (ε_y). All tests are made at three confining pressures (σ_3), 20, 40 and 80 kPa. From these graphs, the identification of the Young's Modulus (E), the Poisson's ratio (ν), the friction angle (φ) and the dilatancy angle (ψ) is calculated.*

Figure 7 shows the typical graphical representation of triaxial test results. In Figure 7a, the deviatoric stress (q_{triax}) is plotted as a function of the vertical strain (ε_y). From the first part of the curve (the elastic part), the Young's modulus (E) can be calculated with Eq. 13 [48].

$$E = \frac{\Delta q_{triax}}{\Delta \varepsilon_y} \qquad \textit{Eq. 13}$$

In Figure 7b, the deviatoric stress (q_{triax}) is plotted against the effective mean stress (p'). The slope (M) of the line linking the three tests provides the internal friction angle (φ), applying the relation Eq. 14 [49].

$$M = \frac{6 \sin \varphi}{3 - \sin \varphi} \qquad \textit{Eq. 14}$$

In Figure 7c, the radial strain (ε_v) is plotted with the vertical strain (ε_y). From the last part of the curve, the angle of dilatancy (ψ) and the Poisson's (ν) coefficient is calculated by means of the expressions Eq. 15 [50] and Eq. 16 [40,51].

$$\sin \psi = -\frac{\varepsilon_v / \varepsilon_y}{2 - \varepsilon_v / \varepsilon_y} \qquad \textit{Eq. 15}$$

$$v = -\frac{\varepsilon_v}{\varepsilon_y} \qquad \textit{Eq. 16}$$

These triaxial tests permit the identification of the Young's Modulus (E), the Poisson's ratio (v), and some parameters for the Drucker-Prager plasticity model: the friction angle (φ) and the dilatancy angle (ψ).

3.2 Characterisation of two abrasive media

Two types of media have been investigated: spherical media (BALL-5 mm) and a pyramidal media (SCT-6 x 6 mm) (Figure 8). The abrasive media were provided by the company *ABCSwissTech*.

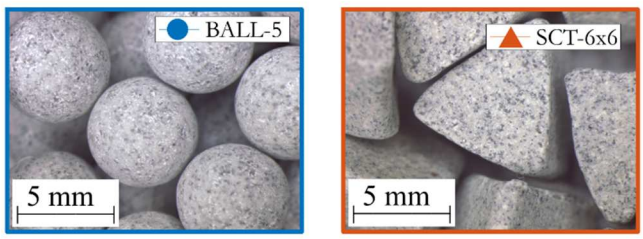

Figure 8. ***Ceramic abrasive media of different shape:*** *a) spherical, Ø=5 mm, and b) pyramidal, dimensions=6x6 mm. Both medias had the same composition and were provided by ABCSwissTech.*

Figure 9 plots the results of triaxial compression tests for both materials at three confining pressures (σ_3). The parameters (E, v, φ and ψ) were extracted from Figure 9 and are reported in Table 2.

It should be noted that the ratio between the yield stress in triaxial tension and that in compression (K) was extracted from the literature [46].

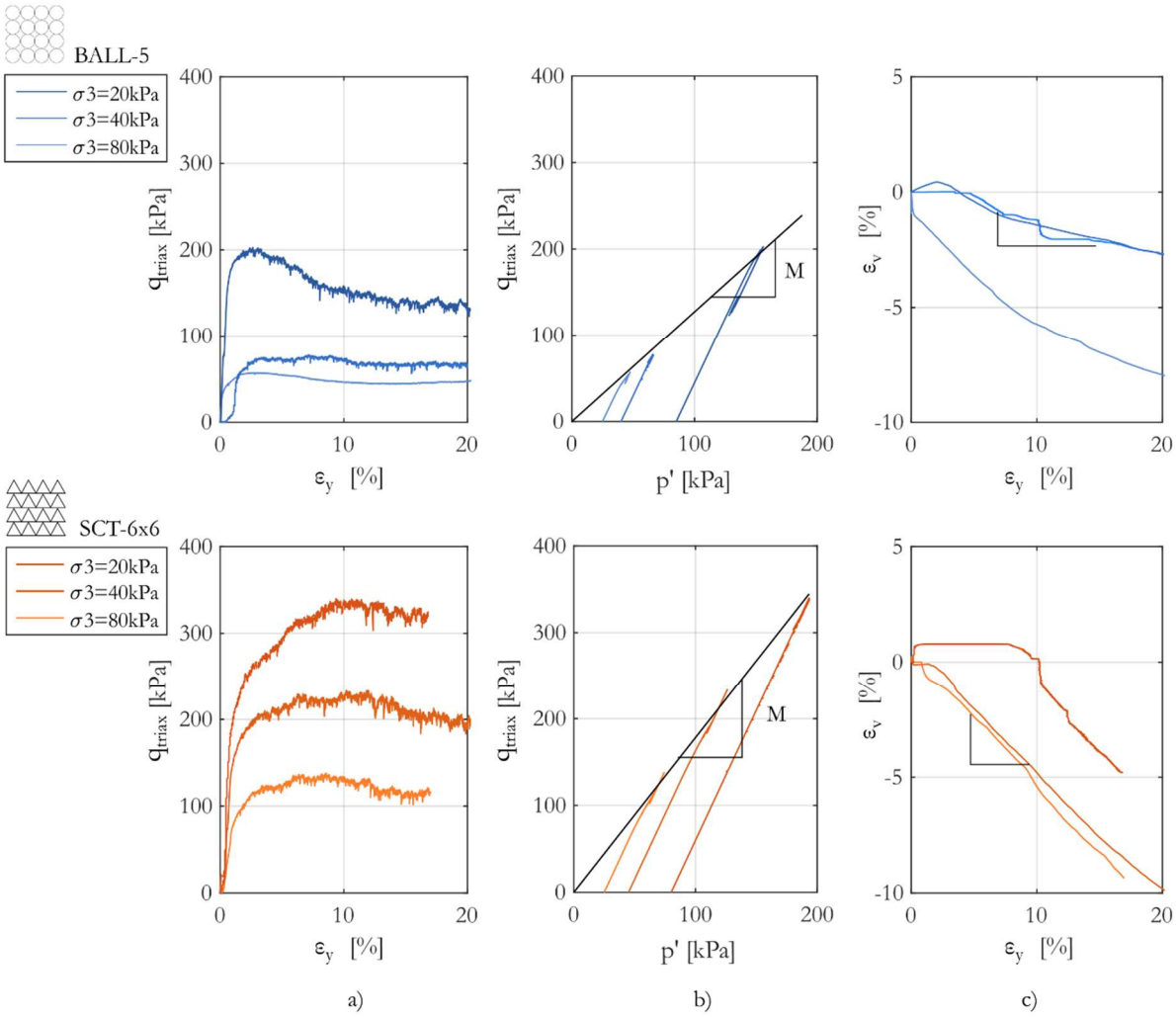

Figure 9. ***Triaxial test results for both media.*** *a) deviatoric stress (q_{triax}) vs. the vertical strain (ε_y), b) deviatoric stress (q_{triax}) vs. the effective mean stress (p') and c) radial strain (ε_v) vs. vertical strain (ε_y) for both medias at different confining stresses (σ_3): 20, 40, 80 kPa.*

Table 2. Material properties of both media.

		Elastic properties		Plastic properties		
	Density (ρ_{bulk}) [kg/m³]	Young's modulus (E) [kPa]	Poisson's ratio (ν)[-]	Internal friction angle (φ) [°]	Dilatency angle (ψ) [°]	Ratio between the yield stress in triaxial tension to compression (K) [-]
BALL-5	1713	179 ± 65	0.3 ± 0.1	31 ± 2	8 ± 3	0.8
SCT 6x6	1489	415 ± 49	0.46 ± 0.07	45 ± 1	13 ± 1	0.8

Figure 9a shows that spherical and pyramidal media exhibit different behaviour. Pyramidal media induces higher levels of deviatoric stress ($q_{triax} \approx 320$ kPa) than spherical media ($q_{triax} \approx 200$ kPa). As far as Young's modulus (E) is concerned, pyramidal media seem to be more rigid ($E \approx 415$ kPa), whereas it is more elastic for spherical media ($E \approx 179$ kPa).

The internal friction angle (φ) of spherical and pyramidal media are estimated (Figure 9b): $\varphi \approx 31°$ and $\varphi \approx 45°$, respectively. Assuming that the local friction coefficient (μ) between surfaces is constant in all cases, because they are composed of the same material, the difference between the internal friction angles of the materials is due to the interlocking between the particles. The pyramidal media have a more angular shape with less capacity to rotate and re-organise under an external force, so the dilation ($l_{2\ SCT6x6} > l_{1\ BALL5}$) is higher, as represented in Figure 10. Pyramidal media exhibit a higher frictional resistance than the spherical ones.

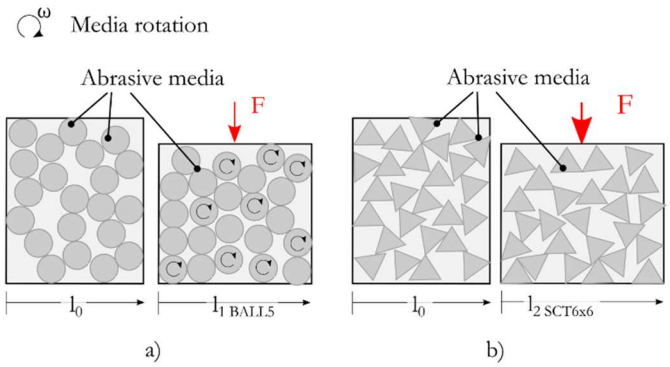

*Figure 10. **Illustration of the interlocking effect of abrasive media.** Both medias are subjected to the same force (F). a) Spherical media have facility to rotate whereas b) pyramidal media do not rotate due to their angular shape.*

From Figure 9c, the dilatancy angle (ψ) is also significantly influenced by the shape of the media. In the case of the pyramidal media, the dilatancy angle (ψ) is higher (13°), whereas it is only 8° for spherical media. This means that this material expands its volume when reorganisation of the particles occurs (as shown in Figure 10). In the same way, the Poisson's ratio (ν) will also be higher in pyramidal media than in spherical media: $\nu \approx 0.45$ and $\nu \approx 0.3$, respectively.

4 Application of the drag finishing model

The objective of this section is to simulate a drag finishing operation using a 2D ALE (Arbitrary Lagrangian Eulerian) model, presented in section 2. The 2D ALE model simulates the flow of abrasive media, considered as a homogeneous and continuous material that interacts with the workpiece to be polished. The behaviour of the material is defined by the continuum plasticity model presented in section 3; the parameters were identified in section 3.2, for both media (spherical and pyramidal). The model provides the mechanical loading parameters (velocity v, normal stress σ_n and shear stress τ) induced for each orientation angle (α) around the cylindrical workpiece (Figure 1).

As this ALE model simulates drag finishing for a defined immersion depth h (and its corresponding hydrostatic pressure (p)), four simulations were launched with two different media (spherical BALL-5 and pyramidal SCT6x6) and two levels of pressure, corresponding to two immersion depths (h=0.07 and 0.12 m), see Table 3. The hydrostatic pressures are calculated with Eq. 1, presented in section 2.

Figure 11 presents an example of numerical results. Figure 11a plots the velocity (v), Figure 11b plots the normal stress (σ_n) and Figure 11c plots the shear stress (τ). The computational time for one simulation of 1 s is around 1 hour, on a single 2.6 GHz CPU and 16 Go of RAM.

Table 3. Simulation information.

N° of simulation	Media	Depth (h) [m]	Pressure (p) [Pa]
1	BALL-5	0.07	1175
2	BALL-5	0.12	2014
3	SCT 6x6	0.07	1021
4	SCT 6x6	0.12	1751

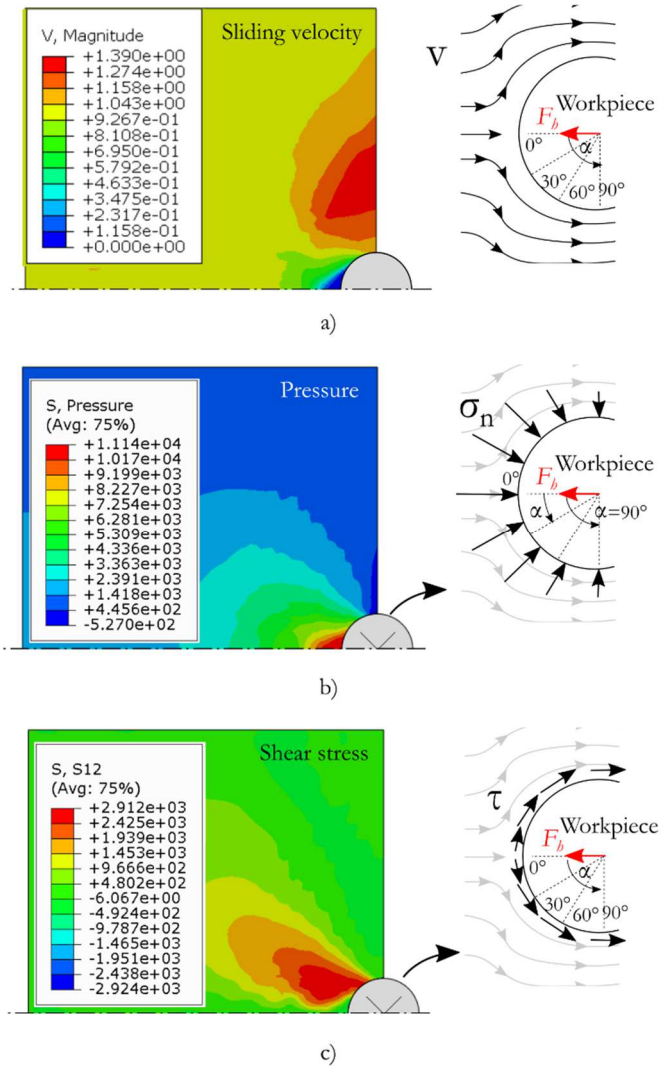

Figure 11. ***Examples of numerical results for case study N°4:*** *a) the sliding velocity (v), b) normal stress (σ_n) and c) shear stress (τ) cartography and distribution around the part. The numerical drag force (F_h) is also indicated in the center of the workpiece.*

4.1 Validation of the numerical model

The development of a model requires validation, based on experimental measurements of the physical parameters. The objective of this section is to compare the experimental drag force ($F_{y\ macro\ exp.}$) applied on the cylindrical workpiece in drag finishing and to compare this value with the one predicted by the numerical model ($F_{y\ macro\ num.}$). This section presents the experimental set-up employed for the drag force ($F_{y\ exp.}$) measurements and, then, presents the procedure to calculate the numerical drag forces ($F_{y\ macro\ num.}$). Finally, experimental and numerical forces are compared.

4.1.1 Experimental drag force measurements

Figure 12a shows an experimental setup developed for measuring the drag force ($F_{y\ macro\ exp.}$) applied on the part that, was inspired by the work of Hashimoto et al. [52] and Zanger et al. [10]. The part was fixed (with no rotation) and the container rotated around its axis. This configuration enabled the part to be held with a force dynamometer (Kistler 9272a) and to record the induced drag forces ($F_{y\ macro\ exp.}$). The container had a diameter of 650 mm and a height of 390 mm. Its rotation speed was adjusted to reach a linear drag velocity of v_{linear}=1 m/s, as in the numerical simulations of section 4. The cylindrical workpiece had a diameter of 20 mm and was 260 mm long.

The container was filled by abrasive media (described in section 3.2) until it reached a specific level (Figure 8). This defined the immersion depth (h) of the workpiece, which is the same as the height of the surface

in contact with the media and, therefore, the hydrostatic pressure (p). The upper surface of the media is flattened by a leveller, so as to maintain a constant contact surface between the workpiece and the media (Figure 12a). Two immersion depths were employed and each test was replicated three times; average values are summarised in Table 4 and plotted in Figure 14.

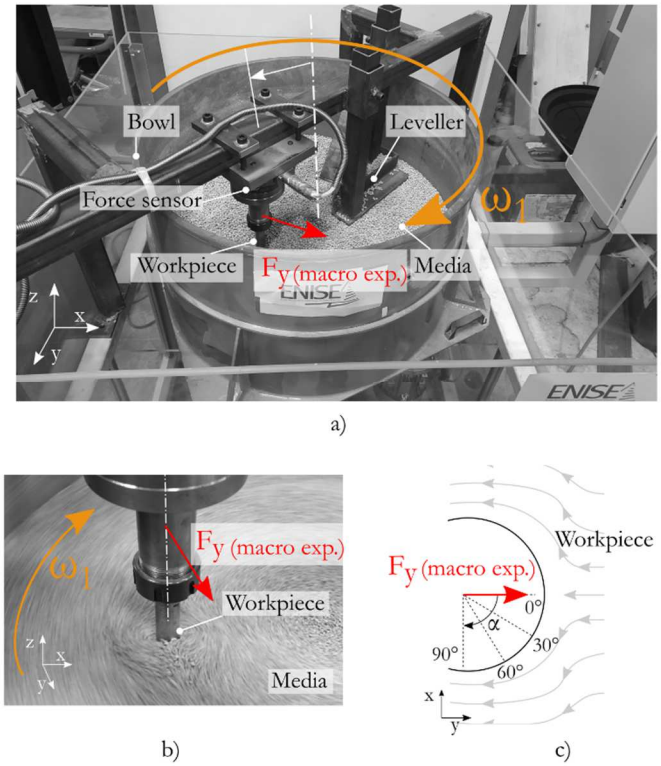

Figure 12. ***The experimental set-up for drag force measurements.*** *a) Developed experimental set-up to measure the macroscopical experimental drag forces ($F_{y\ (macro\ exp.)}$). The components: the bowl or container, the leveller, the media, workpiece and the force sensor are indicated. The container rotates around its own axis with a rotational speed ω_1. In b), a zoom of the media flow around the part is shown and in c) a schematic explanation is shown, indicating media flow and the drag force.*

4.1.2 Numerical drag force measurements

As explained in section 2, the model only takes into account a layer in a specific immersion depth (h_i), see Figure 13a. The hydrostatic pressure (p_i) is applied to the model and the local drag force (F_{hi}) in the workpiece is calculated by the 2D ALE model. It can be considered that the sum of all local drag forces (F_{hi}) calculated at different immersion depths (h_i) matches the macroscopic numerical drag force ($F_{y\ macro\ num.}$), as illustrated in Figure 13b.

However, this method is equivalent to a more simple method, illustrated in Figure 13c. Indeed, the hydrostatic pressure (p_i) depends on the immersion depth (h_i) with a linear equation (the triangle in Figure 13c). It is only necessary to estimate the local drag force (F_h) at the immersion depth h, due to the 2D ALE model. Then, the macroscopic drag force ($F_{y\ macro\ num.}$) is calculated by Eq. 17 in Figure 13c. This was employed to calculate the numerical drag forces ($F_{y\ macro\ num.}$), which are shown in Table 4 and plotted in Figure 14.

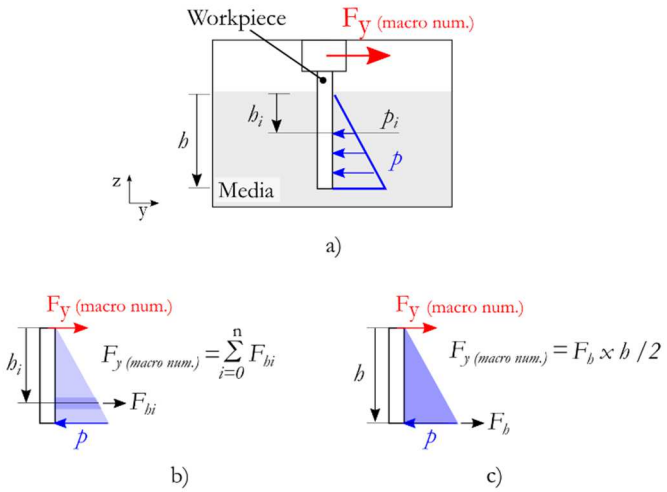

*Figure 13. **Calculation of the numerical force $F_{y\,(macro\ num.)}$.** The schematic drawing of the hydrostatic pressure (p) applied on the workpiece and its resultant force ($F_{y\,(macro\ exp.)}$). At a specific height (h_i), the pressure will be (p_i). In b) and c), two methods to do the transition between the numerical local drag force (F_{hi}) and the numerical macroscopic drag force $F_{y\,(macro\ num.)}$) is proposed.*

$$F_{y\ macro\ num.} = {F_h \cdot h}/{2} \qquad \text{Eq. 17}$$

4.1.3 Comparison between experimental and numerical drag force

Figure 14 plots the experimental and numerical macroscopic drag forces ($F_{y\ macro\ exp.}$, $F_{y\ macro\ num.}$) for two immersion depths (h) and 2 media (BALL-5 and SCT6x6). It shows that the model overestimates drag forces. However, the sensitivity to media and to the immersion depth (h) is well predicted. The higher strength of the pyramidal media clearly leads to higher drag forces. A higher immersion depth (h) also leads to a higher drag force (F_y). The values are reported in Table 4. It is considered that the model provides an acceptable prediction of the drag force. It becomes possible to analyse the mechanical loading parameters (velocity v, normal stress σ_n and shear stress τ) induced for each orientation angle (α) around the cylindrical workpiece.

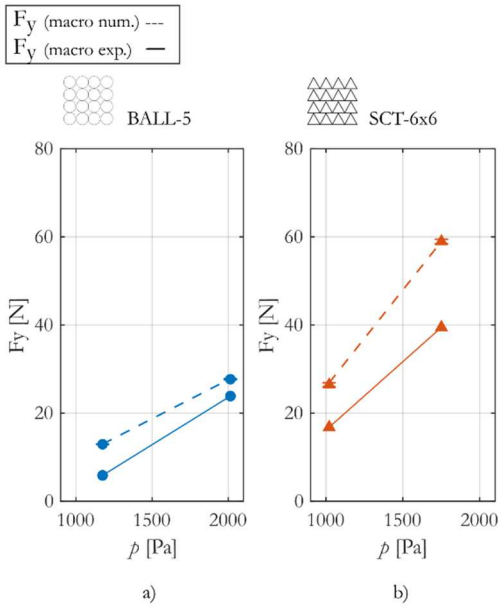

*Figure 14. **Comparison between experimental $F_{y\ macro\ exp.}$ and numerical $F_{y\ macro\ num.}$ drag forces for two immersion depths (h) and two abrasive media:** a) BALL-5 and b) SCT 6x6.*

Table 4. Measured $F_{y\ macro\ exp.}$ and numerically calculated $F_{y\ macro\ num.}$ for two media and two immersion depths (h).

		Experimental results	Numerical results
Abrasive media	*h* [m]	$F_{y\ macro\ exp.}$ [N]	$F_{y\ macro\ num.}$ [N]
BALL-5	0.07	5.8 ± 0.21	12.6 ± 0.04
	0.12	23.8 ± 0.5	26.7 ± 0.11
SCT 6x6	0.07	16.8 ± 1.04	27.4 ± 0.49
	0.12	39.4 ± 0.27	60.4 ± 1.1

4.2 Analysis of the numerical results

Figure 15 plots the sliding velocity (v) around the cylindrical part (orientation angle α), whereas Figure 16 plots the normal stress (σ_n), shear stress (τ) induced in the 'workpiece' surface, at two applied pressures (*p*) corresponding to two immersion depths (*h*). The data series for the spherical media are plotted in blue, whereas those for the pyramidal media are in orange. Tendency curves are drawn with solid lines.

In Figure 15, it appears that the trend is similar, irrespective of media and pressure. At α=0° a stagnation point of the media flow is present. From a macroscopic point of view, the velocity of the material is v ≈ 0 m/s. However, from a mesoscopic point of view, Salvatore et al. [31] proved that media particles are in movement (through a DEM model), even if their velocity is limited. Once passed the stagnation point at α≈15°, the velocity (v) starts increasing until it reaches its maximum value around α≈75°. Near α≈90°, the velocity (v) takes values of v=0 m/s, as the media loses contact with the workpiece. By increasing the hydrostatic pressure (*p*), the area without contact reduces. Figure 15 also reveals that pyramidal media (SCT6x6) leads to higher velocities (v) than spherical ones. On the contrary, the hydrostatic pressure (*p*) does not have a significant influence on velocity.

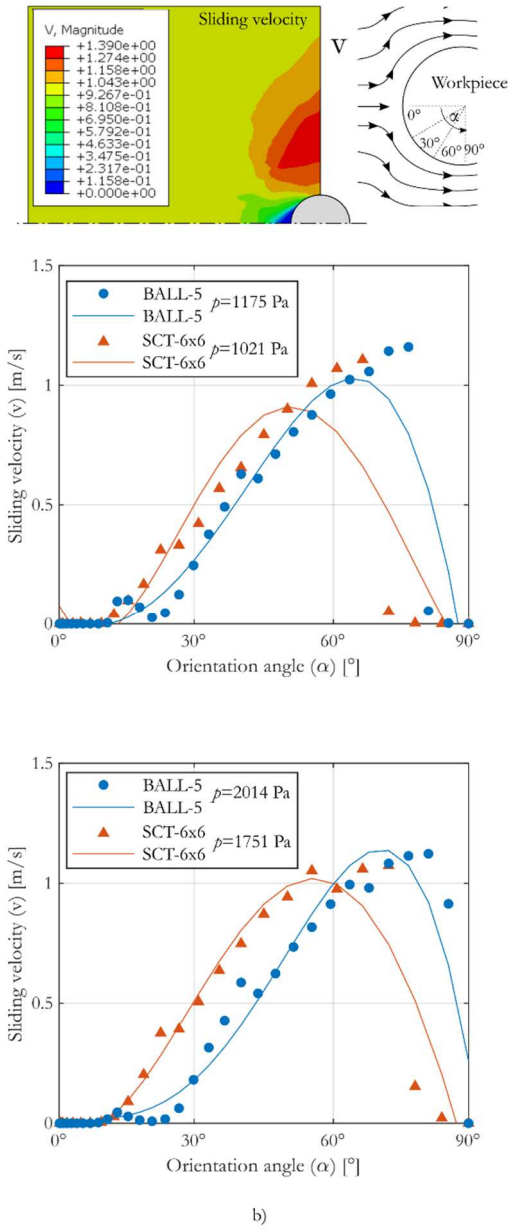

b)

Figure 15. Media sliding velocity distribution around the part (v) for two pressures (p) and two immersion depths (h) for spherical and pyramidal medias.

Figure 16 plots the distribution of normal stress (σ_n) around the part. The normal stress (σ_n) reaches the maximum value in the stagnation point at α=0°. It then decreases as the orientation angle (α) increases, until reaching $\sigma_n \approx 0$ Pa at the lateral side of the part (α=90°). By comparing both media, either in Figure 16a or 16c, it is observed that pyramidal media leads to much higher normal stresses (σ_n) than spherical media. This is due to its higher mechanical resistance: pyramidal media presents higher E, ν, φ, ψ values than the spherical media. The effect of the hydrostatic pressure (p) is visible by comparing Figure 16a and 16c: the higher the pressure (p) applied, the higher the normal stress (σ_n) will be.

As far as the shear stress (τ) is concerned (Figure 16b and 16d), at the stagnation point at α=0°, the shear stress has low values. However, it reaches its maximum value around $\alpha \approx 15°$ in the case of spherical media and around $\alpha \approx 30°$ with the pyramidal ones. Then, the shear stress (τ) decreases towards zero around the lateral side of the part (α=90°). If both media are compared, the pyramidal media leads to much higher shear stress (τ) all around the part, due to its higher mechanical resistance (higher E, ν, φ, ψ than spherical

media, see section 3.2.). Finally, concerning the hydrostatic pressure (p), the comparison between Figure 16b and Figure 16d reveals that the shear stress (τ) is correlated with the pressure (p).

It can be concluded that both normal stress (σ_n) and the shear stress (τ) are strongly dependent on the rheological properties of media and on the hydrostatic pressure (p). On the contrary, the sliding velocity (v) is only influenced by the rheological properties of media but it is not sensitive to the hydrostatic pressure.

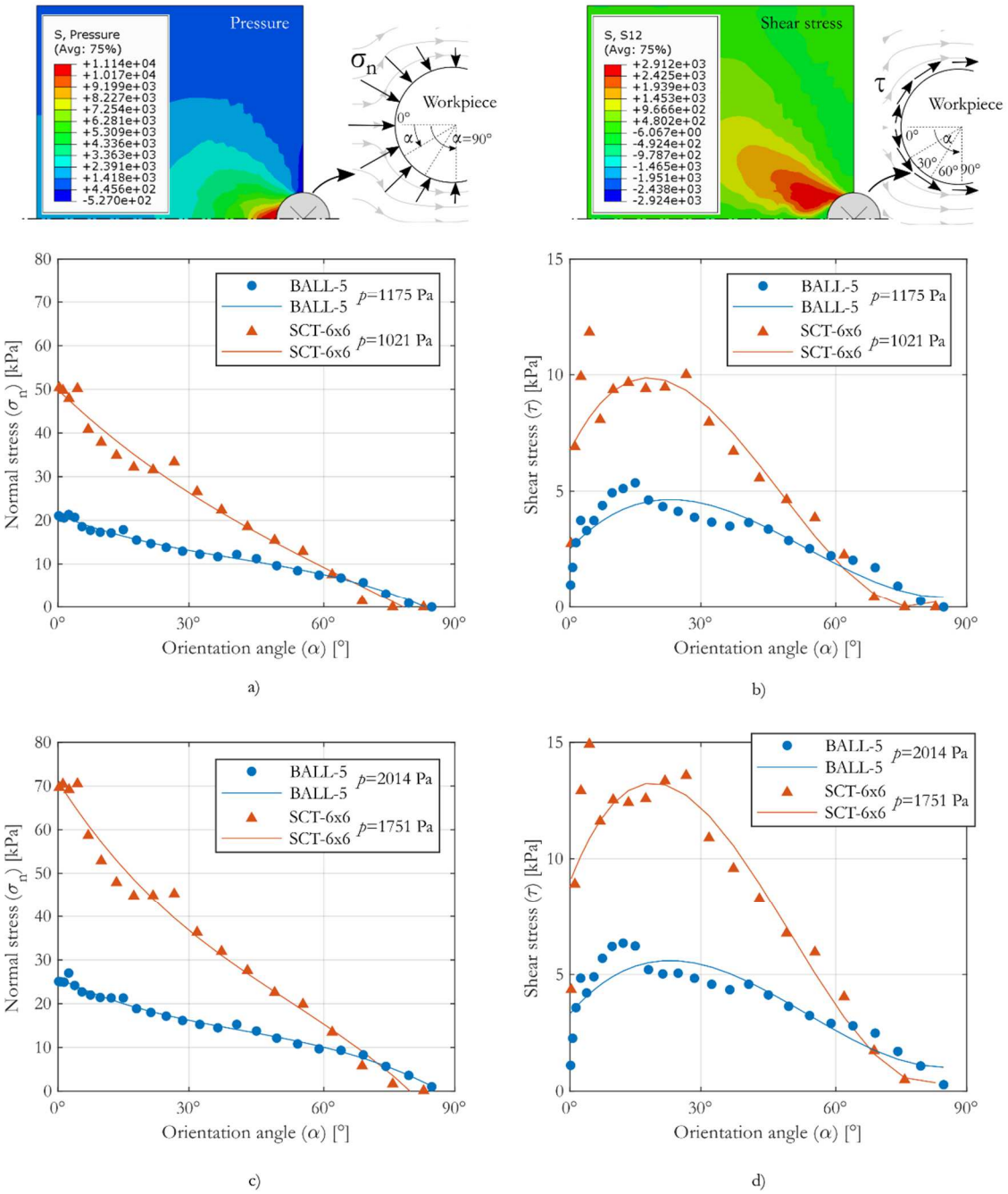

Figure 16. ***The numerical mechanical loading****. a) Normal stress (σ_n) and b) shear stress (τ) distribution around the part for two hydrostatic pressures (p) and two immersion depths (h) for spherical and pyramidal medias.*

5 Evolution of surface roughness in drag finishing

This section aims to investigate the evolution of surface roughness in drag finishing for the two abrasive media involved in this paper (Figure 8). Drag finishing tests were conducted with the experimental set-up presented in Figure 12.

5.1 Materials and Methods

Cylindrical samples were manufactured with a ferritic-pearlitic mild steel (AISI1045). Its diameter was 20 mm and its height was 80 mm (Figure 17a). A calibrated surface roughness was machined by the milling process presented in Figure 17b. The turn-milling conditions are reported in Table 5. Figure 17c illustrates the surface topography (3D), Figure 17d shows an example of the surface profile (2D) and indicates the roughness parameters: Ra~12 µm, RSm~105 µm and Rsk~1.5.

With regard to drag finishing conditions, 175 kg of the spherical and pyramidal media that were considered previously, in sections 3 and 4, were used in the drag finishing process. In addition, a liquid compound was added: a passive alkaline liquid, with pH~8 (Ref: Pulibrill 6140, *ABC SwissTech*) and 5% concentration. The set-up was connected to a filtering machine, to remove debris with a flow rate of 5 l/min. The workpiece was dragged through the media and liquid compound with a constant linear velocity of v_{linear}=1 m/s and the analysed surfaces were immersed at h=0.07 m.

Table 5. Milling process parameters.

Milling tool	MC232-06.0W2B-WJ30ED Walter
Cutting speed (Vc [m/min])	200
Number of teeth	2
Feed per tooth (f_z [mm])	0.05
Axial depth of cut (a_p [mm])	0.07
Radial depth of cut (a_e [mm])	0.07
Lubrication	Emulsion
Workpiece inclination [°]	45
Step over distance [µm]	100
Scallop height [µm]	50

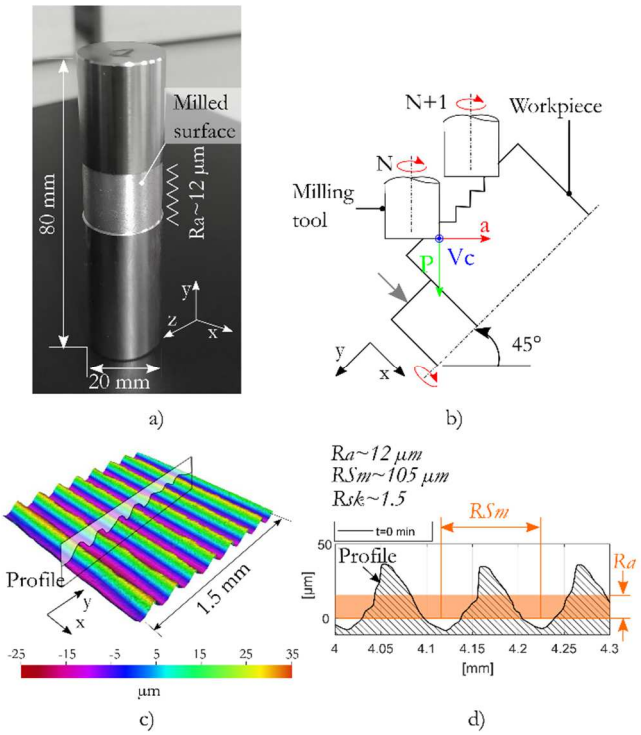

Figure 17. ***Sample fabrication and characteristics.*** *a) Sample shape and dimensions with a milled surface of Ra=12 µm, b) milling process used to create the periodical surface, c) the details of the periodical surface in 3D, and d) its surface profile in 2D and Ra, RSm and Rsk values.*

Surface topography characterisations were carried out using a focus variation microscope (*Alicona Infinite Focus*). Each surface had a dimension of 5 mm along the axis of the sample (y in Figure 18a), and 1.5 mm in the circumferential direction (x-z plane). A magnification of 20x was applied and the corresponding vertical and lateral resolutions were 2.5 µm and 0.1 µm, respectively. Four main areas were measured at 0, 30, 60 and 90° with regard to media flow (in the z axis) (Figure 18a) during the drag finishing process at time intervals of t=0, 5, 20, 60, 120, and 210 min. The measured topographies were then post-processed with the MountainMaps® commercial software. From the main surface (5 x 1.5 mm), a section (1.5 x 1.5 mm) was selected to calculate the arithmetical mean deviation of roughness (*Sa*) as shown in Figure 18b.

In addition to the analysis of surface roughness parameters, it is also important to follow the position of the profile. Analysis of the position permits us to deduce the amount of material that was removed by cutting or that was plastically deformed during the finishing process. If the final profile is below the original profile, this means that cutting was the dominant mechanism. On the contrary, the final profile remains in the middle of the original profile and this means that plastic deformation was the dominant mechanism. In practice, a 2D profile (in the Y direction) was extracted from the measured surfaces (5 x 1.5 mm). Initial and final surface profiles were superimposed on the same reference (Figure 18b), which was created by indenting the surfaces with a cone indenter. During the drag finishing process, the valley of the indentation area remained intact because its width (<1 mm) was narrower than the employed minimum media diameter (~5 mm). So, it becomes possible to locate the position of the two profiles before and after the process.

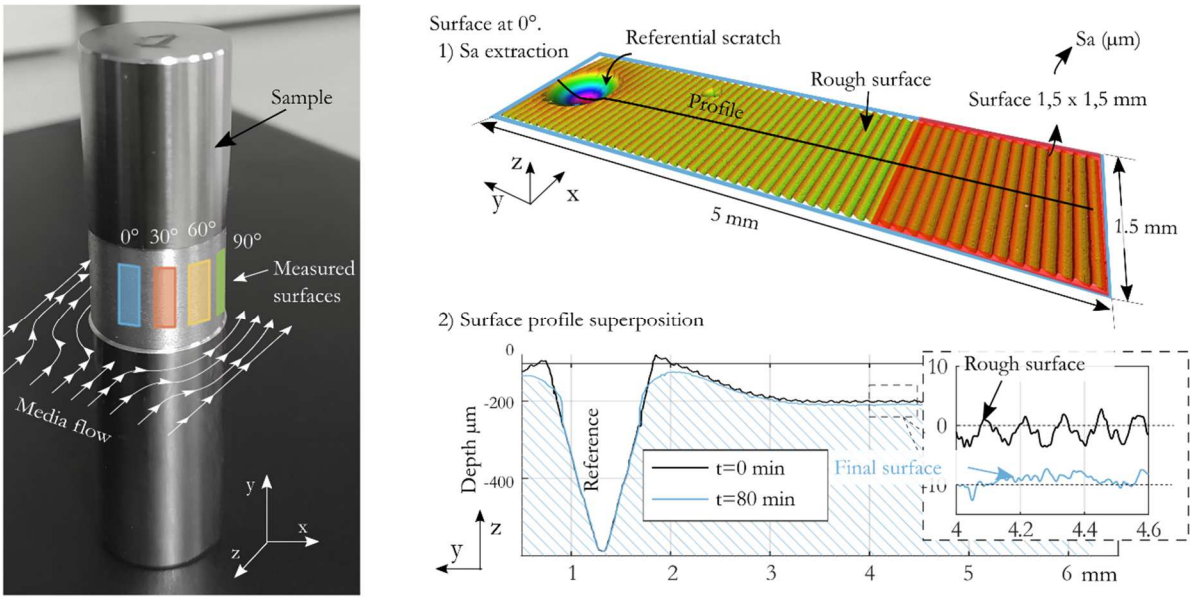

Figure 18. ***Surface topography analysis****. a) The sample with the milled surface. The measured surfaces positions are indicated in different colours. Media flow is drawn with white arrows. At b) the surface at 0° is shown with its dimensions and the referential scratch. The section from Sa is calculated is indicated in red colour, and the extracted surface profile in black. Finally, at c), surface profile superposition is made using the referential scratch. The gap between the rough surface and the final surface shows how many material was removed in tribofinishing.*

5.2 Experimental results

Figure 19 shows the evolution of *Sa* and Figure 20 presents the superposition of primary profiles before and after drag finishing for both abrasive media and four surface orientation angles (α).

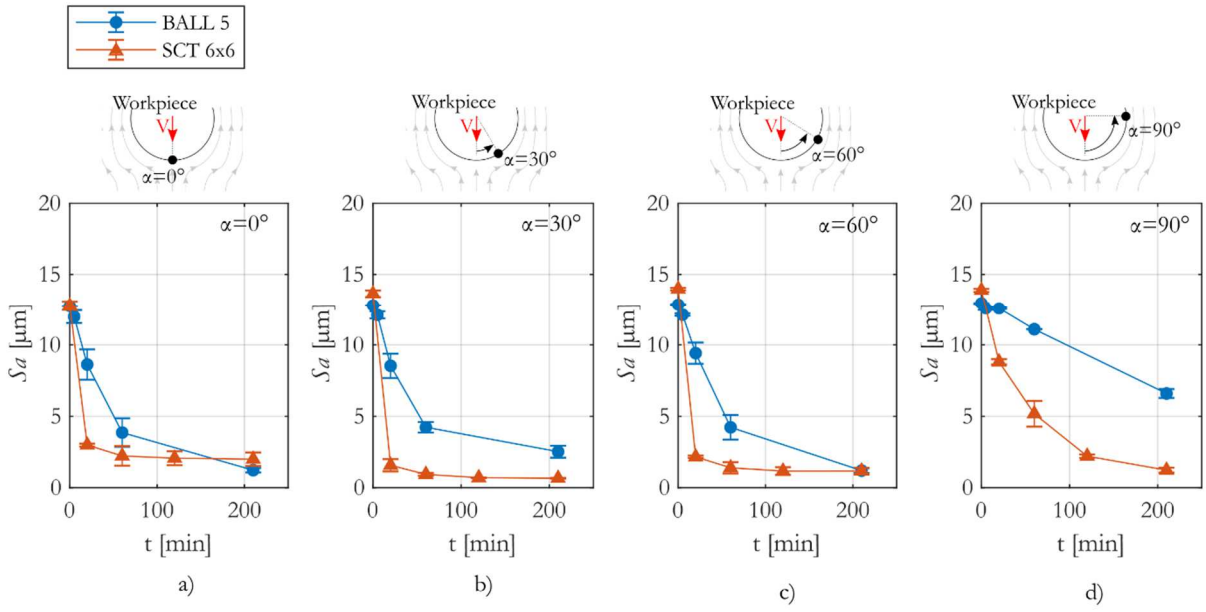

Figure 19. ***Sa evolution graphs.*** *Sa after 210 min of drag finishing for both abrasive media (BALL5 and SCT 6x6) at four surface orientations (α) a) 0°, b) 30°, c) 60° and d) 90°.*

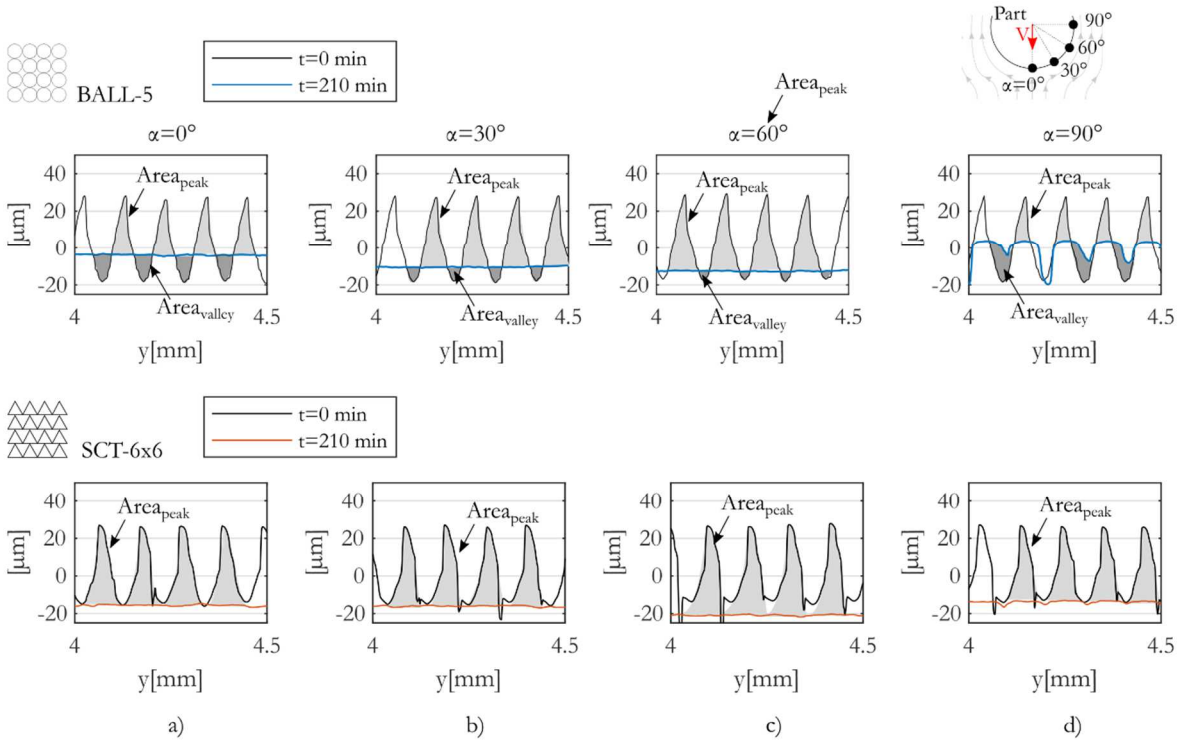

Figure 20. ***Initial and final (t=210 min) primary profiles.*** *For surfaces polished with BALL-5 and SCT 6x6 at four surface orientations (α): a) 0°, b) 30°, c) 60° and d) 90°. Peak and valley areas are indicated in grey colours ($Area_{peak}$ and $Area_{valley}$).*

Concerning the evolution of surface roughness (*Sa*) and, more precisely, the slope of the curves, it can be seen that the pyramidal media (orange) is more effective than spherical media (blue) to reduce surface roughness (*Sa*). This is observable for any surface orientations (α). However, it is clear that the evolution of the roughness (*Sa*) depends on orientation angle (α). It seems that, as far as pyramidal media are concerned, the most efficient orientation angle is α=30 to 60°. On the contrary, spherical media leads to similar roughness values (*Sa*) in the range α=0 - 60°.

At the end of the drag finishing tests (t=210 min), the roughness values (*Sa*), reached by both abrasive media, were quite similar for the orientation angles (α) at 0, 30 and 60°. On the contrary, on the lateral side and parallel to the media flow (α=90°), spherical media were not that efficient in decreasing surface roughness (Figure 19d).

This analysis has to be completed with the analysis of the final surface profiles in Figure 20 in order to conclude what type of interaction mechanism happened (abrasion or plastic deformation). Figure 20 defines the parameter (A_{peak}) corresponding to the area between the original profile over the final profile. This parameter represents a quantity of work material. Figure 20 also defines the parameter (A_{valley}), corresponding the area between the original profile below the final profile. This parameter illustrates a free volume (no material). As the original profiles were almost triangular, it is possible to analyse the ratio between A_{peak} / A_{valley}. When A_{peak} is equivalent to A_{valley}, this shows that plastic deformation was the dominant mechanism and no work material has been removed. The final profile is in the middle of the original profile. On the contrary, when A_{peak} is much larger than A_{valley}, this reveals that cutting or abrasion was the dominant mechanism and the final profile is shifted below. In this extreme situation, when A_{valley} is equal to zero, the original profile has been fully removed by abrasion, which reveals a high efficiency of the drag finishing process.

It is also possible to define the parameter MR (material removal) by using Eq. 18. This indicator (MR) reveals the amount of material that has been removed for a defined orientation angle (α).

Finally, the parameter PD (plastic deformation ratio) is defined by Eq. 19. When plastic deformation is the single mechanism, PD is closer to 1. On the contrary, when PD is equal to zero, abrasion is the single mechanism.

$$MR = A_{peak} - A_{valley} \quad \text{Eq. 18}$$

$$PD = A_{valley} / A_{peak} \quad \text{Eq. 19}$$

Table 6. A_{peaks}, A_{valley} MR and PD for both media and all orientation angles (α).

Abrasive media	α [°]	A_{peak} [µm²]	Av_{alley} [µm²]	MR [µm²]	PD [-]
BALL-5	0	860	161	699	0.19
	30	1326	142	1183	0.11
	60	1751	122	1628	0.07
	90	500	30	470	0.06
SCT 6x6	0	2215	0.00	2215	0
	30	2259	0.00	2259	0
	60	2354	0.00	2354	0
	90	1674	0.00	1674	0

In Figure 20a, at α=0°, the position of the final profile differs between pyramidal and spherical media. The orange line, corresponding to the profile generated by pyramidal media, is below the original profile, in black. A_{peak} is much bigger than A_{valley} (=0). This shows that a large amount of material has been removed by abrasion. On the contrary, the blue line, corresponding to the final profile generated by the spherical media, remains in the middle of the original profile. A_{peak} is only slightly bigger than A_{valley}. This means that the material on the peaks was plastically deformed until filling the valleys. It can be concluded that plastic deformation was the dominant mechanism. However, a small amount of material has been removed, as the parameter MR is significantly higher than zero: MR ~ 699 mm². This shows that plastic deformation was the dominant mechanism in this area, even though some material had been removed. It should be noted that the final surface roughnesses *(Sa)* are very similar after 210 min, as shown in Figure 19a. So, this analysis illustrates the necessity to combine the analysis of surface roughness parameters and profiles, in order to understand the fundamental mechanisms in drag finishing.

By analysing the profiles at α=30°, a similar analysis can be made. Pyramidal media remains the most efficient way to remove the material by abrasion (scratching), whereas spherical media have a dominant plastic action. However, the parameter MR becomes greater, which reveals that a larger amount of material has been removed. So, the balance between plasticity and abrasion is modified for spherical media.

This trend remains for the orientation angle α=60°. The parameter A_{valley} becomes very small for the spherical media. The parameter MR increases. For both media, scratching becomes the dominant mechanism. As far as pyramidal media is concerned, it is observable that the orange line is significantly below the original profile, which shows its highest efficiency to remove material for this orientation angle.

In the lateral zone (α=90°), the situation becomes different. The spherical media leads to a plateau profile with a large decrease of peaks, whereas valleys are not that affected. This shows that scratching becomes the dominant mechanism. Unfortunately, the MR is low which shows that this media is inefficient in this area. On the contrary, pyramidal media keep their efficiency.

As a summary, this section shows the necessity to combine the analysis of surface roughness parameters and profiles in parallel, so as to understand the fundamental mechanisms in drag finishing. It has been revealed that spherical media promotes plastic deformation at low orientation angles, whereas it promotes

scratching for high orientation angles. As far as surface roughness is concerned, the efficiency of spherical media decreases for high orientation angles. On the contrary, pyramidal media promotes scratching mechanisms for the whole range of orientations, even if its maximum efficiency is observable for α=60°.

6 Correlation between physical parameters and surface roughness

This section aims to compare the physical parameters (τ, σ_n, v) quantified in the numerical simulations, with the surface topography obtained during the experimental tests. Figure 21 summarises both the experimental results and the numerical ones. The investigated experimental parameters were: 1) the surface roughness change (ΔSa) and 2) the predominant mechanism (material removal (MR) or plastic deformation (PD)) at t=210 min in four surface orientations (α), see Figures 21a, 21b, 21c and 21d. The investigated numerical parameters were: 3) the normal stress (σ_n) and the shear stress (τ) on the surface, and 4) the sliding velocity (v) (see Figure 21e and 21f). In addition, Figure 21g and 21h plot the evolution of the shear stress multiplied by the sliding velocity (τ x v) that represents a shearing energy at the interface.

Spherical media

Figure 21a shows that, during the polishing with the spherical media (BALL-5), ΔSa is different in each surface orientation (α). According to Figure 21c, a combination of plastic deformation and material removal happened. At α=0° almost only plastic deformation occurs, whereas at α=30° and 60° both phenomena are combined. The material removal (MR) mechanisms (abrasion, scratching) become the predominant phenomena. Finally, at α=90°, only material removal takes place.

If the mechanical loading is observed in Figure 21e, the frontal zone (α=0°) is subjected to high normal stress (σ_n), low shear stress (τ) and low sliding velocities (v). This leads to plastic deformation, as Saljé [53] stated. However, a small amount of material removal occurs too, which can be attributed to the erosion due to the rotation of spherical media around themselves during the flow, as well as the small velocity at the mesoscopic scale, as shown by Salvatore et al. [31]. In between (α=30-60°), surfaces withstand a combination of intermediate intensities of normal and shear stresses (σ_n, τ) and sliding velocities (v). All of the mechanisms (plastic deformation, ploughing and scratching) can be activated, depending on the magnitude of the normal and shear stress (σ_n, τ) and sliding velocities, as stated by [37,54]. Preston [33] and Yingjie et al. [55] showed that maximum wear can be seen when simultaneously combining high normal stresses (σ_n) and velocities (v). Figure 21g shows the multiplication of (τ x v) as a function of surface orientation (α). The curve is compared to the experimental results, ΔSa in Figure 21a and 21c. It can be observed that the highest point of the curve (τ x v) corresponds to the highest ΔSa and highest MR values. Finally, the surface at α=90° was subjected to low stresses (τ, σ_n) and it can be seen (in section 4) that the contact between media and the workpiece were not assured. When both parts are in contact, media have high velocities and, even if τ, and σ_n are low, pure material removal of the roughness peaks occurs (i.e. ploughing or scratching).

Pyramidal media

Concerning the media polished with the pyramidal media (SCT6x6), material removal (MR) is very high for all surface orientations (α). The final profile is positioned below the valleys of the initial profile and the variation of surface roughness ΔSa is compared to spherical media. In addition the plastic deformation indicator, DP is zero. This high efficiency of the pyramidal media can be explained by:

1) the normal stress (σ_n) and the shear stress (τ) are much higher than for spherical media (Figure 21a vs. 21b).

2) the cutting efficiency of the pyramidal media, as it is assumed that pyramidal media creates smaller contact surfaces with the workpiece due to its sharp edges at a microscopic scale (Figure 1c), inducing

655 higher local stresses and penetrating the surface at this microscopic scale; more damage and material
656 removal occurs [30,34].

657 No remarkable difference are noticed between surface orientations (α) if only the final surfaces (ΔSa) are
658 observed. However, roughness evolution (Sa) in Figure 19 reveals that the most efficient conditions are at
659 α=30° and 60° as roughness (Sa) reduces rapidly and MR reaches its maximum value. This is because of
660 the high normal stresses (σ_n) combined with high sliding velocities (v) (see Figure 21h), which leads to
661 higher rates of material removal [33,55].

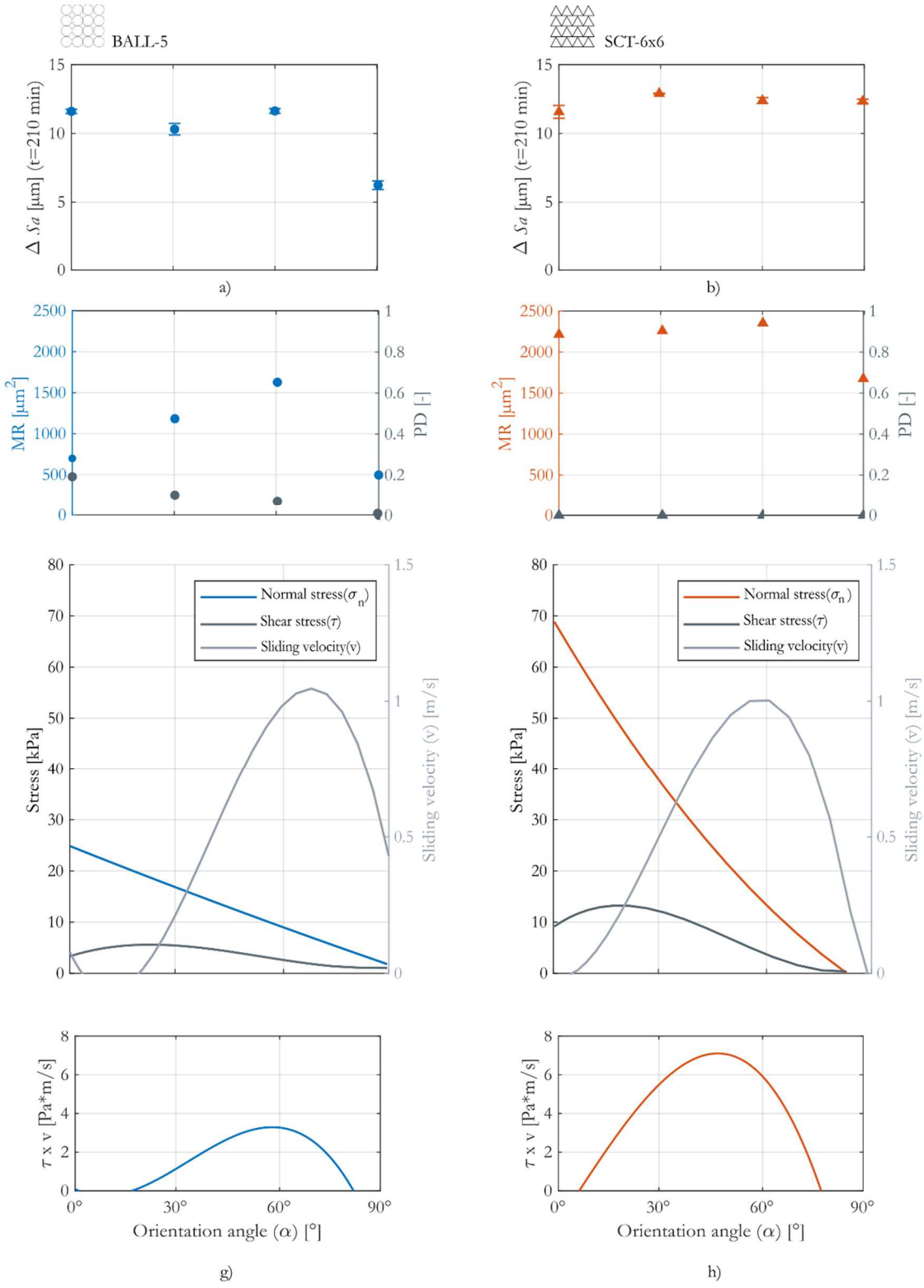

Figure 21. ***Correlation between experimental and numerical results.*** *Experimental surface roughness difference (ΔSa) depending on the orientation angle (α) for a) spherical and b) pyramidal medias. Material removal and plastic deformation mechanisms for each orientation angle and each abrasive media: c) spherical and d) pyramidal medias. In e), f), the numerical mechanical loading (sliding velocity, v, normal σ_n and shear stresses τ) are shown for both abrasive medias. Finally, in g) and h), the shearing energy is calculated to show the optimal orientation angle.*

The mechanical loading extracted from these numerical simulations at a macroscopic scale were correlated with the reduced surface roughness (Δ*Sa*) and the material removal (MR) or plastic deformation (DP)

mechanism. The macroscopic loads were able to explain the observed experimental phenomena. This means that the macroscopic loads are directly related to the evolution of surface roughness at a microscopic scale. As a summary, Figure 22 shows the mechanisms that are more likely to occur in each zone.

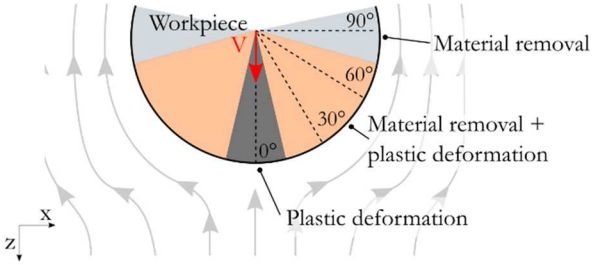

Figure 22. ***Interaction mechanisms during drag finishing.*** *Plastic deformation and material removal mode regions as a function of surface orientation angle (α) regarding media flow (grey arrows).*

7 Conclusions

This paper has proposed a model that simulates the abrasive media flow around a part during the drag finishing process. The present paper is focused on modelling drag finishing at a macroscopic scale.

The first major contribution of this work consists of proposing a model that simulates the flow of abrasive media, considered as a homogeneous and continuous material around a workpiece, as well as its interaction with a workpiece. This is a new numerical model of drag finishing based on an ALE (Arbitrary Lagrangian Eulerian) formulation. The model permits calculation of the mechanical loadings (velocity, normal stress and shear stresses) induced around the part and correlates these physical parameters to the evolution of surface roughness, which brings a better understanding of the mechanisms (plastic deformation or abrasion) controlling the efficiency of the drag finishing process. This model has the potential to be generalised for any complex parts.

The second major contribution of this paper is to bring a contribution to the characterisation of the macroscopic rheological properties of abrasive media. The so-called 'triaxial test' is proposed, based on the field of soil mechanics, to identify the Drucker Prager plasticity model. This test can be applied to any abrasive media. It has the potential to provide global trends on the effect of media (geometry, size, lubricant) on the rheological properties of granular materials.

In addition, as the development of a numerical model requires an experimental validation, an original experimental set-up enables us to measure the macroscopic drag force applied on the part.

The ALE model, the identification of the rheological model and the experimental validation have been applied to investigate the drag finishing process of a cylindrical part made of AISI1045 steel, with two kinds of abrasive media (spherical and pyramidal). It has been shown that:

- Pyramidal media exhibit significantly higher rheological behaviour compared to spherical media (φ_{BALL5}=31° < φ_{SCT66}=45°), that is mainly attributed to the interlocking effect between each media. This effect is due to the geometry of the particles: particles lock among themselves providing a higher resistance towards deformation. So, the geometry of abrasive media seems to be the main factor influencing its macroscopic rheological behaviour.
- Experimental and numerical drag forces were compared to validate the numerical model. It has been shown that the model enables the prediction of drag forces with reasonable agreement. The sensitivity of the drag force to media rheology (i.e. the internal friction angle, φ) and the immersion depth (h) is well predicted. Drag forces were 126 % higher for pyramidal media than the spherical ones and 53 % higher for an immersion depth of h=0.12 m in the case of pyramidal media.

- The model provides relevant mechanical parameters such as the distribution of stresses (normal and shear stresses) and sliding velocities at the interface between abrasive media and the surface to be polished. The model has been applied to simulate the same two abrasive media. It has been shown that pyramidal media leads to much higher normal and shear stresses (180 % and 106 % higher respectively), whereas sliding velocities are only slightly higher, compared to spherical media. The model has also highlighted that the immersion depth of the part (*h*), i.e. the hydrostatic pressure, affects the normal and shear stresses (40 % and 35 % higher in the case of pyramidal media), whereas it has almost no influence on the velocity of media.
- The correlation between experimental drag finishing tests and numerical test results reveals the physical mechanisms at the interface between the media and the surface. It was highlighted that spherical media, combined with a small orientation angle, promote plastic deformation phenomena, whereas higher orientation angles facilitate cutting mechanisms. On the contrary, pyramidal media promote cutting mechanisms irrespective of the orientation angle, due to the more aggressive contact between angular media and the surface roughness at a microscopic scale. Moreover, it has been shown that the efficiency of both media is optimised for an inclined orientation angle between 30° and 60°, where a combination of shear stress and sliding velocity leads to a maximum shearing energy.

References

[1] Gillespie, L. K., 2007, Mass Finishing Handbook. New York: Industrial Press Inc.

[2] Yang, S., Li, W., 2018, Surface Finishing Theory and New Technology. Berlin, Heidelberg: Springer Berlin Heidelberg.

[3] Khan, H. M., Sirin, T. B., Tarakci, G., Bulduk, M. E., Coskun, M., et al., 2021, Improving the surface quality and mechanical properties of selective laser sintered PA2200 components by the vibratory surface finishing process, SN Applied Sciences, 3/3:364, DOI:10.1007/s42452-021-04371-4.

[4] Atzeni, E., Balestrucci, A., Catalano, A. R., Iuliano, L., Priarone, P. C., et al., 2020, Performance assessment of a vibro-finishing technology for additively manufactured components, in *Procedia CIRP*, pp. 427–432.

[5] Nutal, N., Rochus, P., Collette, J., Crahay, J., Jochem, H., et al., 2015, Surface engineering for parts made by additive manufacturing, in *66th International Astronautical Congress*.

[6] Witkin, D. B., Patel, D. N., Helvajian, H., Steffeney, L., Diaz, A., 2018, Surface Treatment of Powder-Bed Fusion Additive Manufactured Metals for Improved Fatigue Life, Journal of Materials Engineering and Performance, pp. 1–12, DOI:10.1007/s11665-018-3732-9.

[7] Jamal, M., Morgan, M., 2017, Design Process Control for Improved Surface Finish of Metal Additive Manufactured Parts of Complex Build Geometry, Inventions, 2/4:36, DOI:10.3390/inventions2040036.

[8] Kacaras, A., Gibmeier, J., Zanger, F., Schulze, V., 2018, Influence of rotational speed on surface states after stream finishing, in *Procedia CIRP*, pp. 221–226.

[9] Barletta, M., Pietrobono, F., Rubino, G., Tagliaferri, V., 2014, Drag finishing of sensitive workpieces with fluidized abrasives, Journal of Manufacturing Processes, 16/4:494–502, DOI:10.1016/J.JMAPRO.2014.06.003.

[10] Zanger, F., Kacaras, A., Neuenfeldt, P., Schulze, V., 2019, Optimization of the stream finishing process for mechanical surface treatment by numerical and experimental process analysis, CIRP Annals, 68/1:373–376, DOI:10.1016/J.CIRP.2019.04.086.

[11] Uhlmann, E., Dethlefs, A., Eulitz, A., 2014, Investigation of Material Removal and Surface Topography Formation in Vibratory Finishing, Procedia CIRP, 14:25–30,

754 DOI:10.1016/J.PROCIR.2014.03.048.

755 [12] Malkorra, I., Salvatore, F., Arrazola, P. ., Rech, J., 2020, The influence of the process parameters of
756 drag finishing on the surface topography of aluminium samples, CIRP Journal of Manufacturing
757 Science and Technology.

758 [13] Song, X., Chaudhari, R., Hashimoto, F., 2014, Experimental Investigation of Vibratory Finishing
759 Process, in *Volume 2: Processing*, p. V002T02A013.

760 [14] Ciampini, D., Papini, M., Spelt, J. K. K., 2007, Impact velocity measurement of media in a
761 vibratory finisher, Journal of Materials Processing Technology, 183/2–3:347–357,
762 DOI:10.1016/J.JMATPROTEC.2006.10.024.

763 [15] Malkorra, I., Salvatore, F., Rech, J., Arrazola, P. J., Tardelli, J., et al., 2020, Influence of lubrication
764 condition on the surface integrity induced during drag finishing, in *CIRP CSI*.

765 [16] Domblesky, J., Evans, R., Cariapa, V., 2004, Material removal model for vibratory finishing,
766 International Journal of Production Research, 42/5:1029–1041,
767 DOI:10.1080/00207540310001619641.

768 [17] Rech, J., Giovenco, A., Courbon, C., Cabanettes, F., 2018, Toward a new tribological approach to
769 predict cutting tool wear, CIRP Annals, 67/1:65–68, DOI:10.1016/j.cirp.2018.03.014.

770 [18] Dražumerič, R., Badger, J., Roininen, R., Krajnik, P., 2020, On geometry and kinematics of
771 abrasive processes: The theory of aggressiveness, International Journal of Machine Tools and
772 Manufacture, 154:103567, DOI:10.1016/j.ijmachtools.2020.103567.

773 [19] Huang, A. N., Kuo, H. P., 2017, CFD simulation of particle segregation in a rotating drum. Part I:
774 Eulerian solid phase kinetic viscosity, Advanced Powder Technology, 28/9:2094–2101,
775 DOI:10.1016/j.apt.2017.05.016.

776 [20] Cariapa, V., Park, H., Kim, J., Cheng, C., Evaristo, A., 2008, Development of a metal removal
777 model using spherical ceramic media in a centrifugal disk mass finishing machine, The
778 International Journal of Advanced Manufacturing Technology, 39/1–2:92–106,
779 DOI:10.1007/s00170-007-1195-5.

780 [21] Zheng, Q. J., Yu, A. B., 2015, Modelling the granular flow in a rotating drum by the Eulerian finite
781 element method, Powder Technology, 286:361–370, DOI:10.1016/j.powtec.2015.08.025.

782 [22] Hashemnia, K., Spelt, J. K. J. K., 2015, Finite element continuum modeling of vibrationally-
783 fluidized granular flows, Chemical Engineering Science, 129:91–105,
784 DOI:10.1016/j.ces.2015.02.025.

785 [23] Johnson, P. C., Jackson, R., 1987, Frictional-collisional constitutive relations for granular materials,
786 with application to plane shearing, Journal of Fluid Mechanics, 176:67–93,
787 DOI:10.1017/S0022112087000570.

788 [24] M.Das, B., 2008, Advanced soil mechanics. .

789 [25] Kaliakin, V. N., 2017, Soil Mechanics Calculations, Principles, and Methods. Elsevier Butterworth-
790 Heinemann.

791 [26] Li, X., Li, W., Yang, S., Hao, Z., Shi, H., 2018, Study on polyurethane media for mass finishing
792 process: Dynamic characteristics and performance, International Journal of Mechanical Sciences,
793 138–139:250–261, DOI:10.1016/j.ijmecsci.2018.02.017.

794 [27] Ngo, N. T., Indraratna, B., Rujikiatkamjorn, C., 2017, Micromechanics-Based Investigation of
795 Fouled Ballast Using Large-Scale Triaxial Tests and Discrete Element Modeling, Journal of
796 Geotechnical and Geoenvironmental Engineering, 143/2:04016089, DOI:10.1061/(asce)gt.1943-
797 5606.0001587.

798 [28] Naeini, S. E. E., Spelt, J. K. K., 2009, Two-dimensional discrete element modeling of a spherical

steel media in a vibrating bed, Powder Technology, 195/2:83–90, DOI:10.1016/j.powtec.2009.05.016.

[29] Uhlmann, E., Eulitz, A., Dethlefs, A., 2015, Discrete element modelling of drag finishing, in *Procedia CIRP*, pp. 369–374.

[30] Uhlmann, E., Dethlefs, A., Eulitz, A., 2014, Investigation into a geometry-based model for surface roughness prediction in vibratory finishing processes, International Journal of Advanced Manufacturing Technology, 75/5–8:815–823, DOI:10.1007/s00170-014-6194-8.

[31] Salvatore, F., Grange, F., Kaminski, R., Claudin, C., Kermouche, G., et al., 2017, Experimental and Numerical Study of Media Action During Tribofinishing in the Case of SLM Titanium Parts, Procedia CIRP, 58:451–456, DOI:10.1016/J.PROCIR.2017.03.251.

[32] Makiuchi, Y., Hashimoto, F., Beaucamp, A., 2019, Model of material removal in vibratory finishing, based on Preston's law and discrete element method, CIRP Annals, 68/1:365–368, DOI:10.1016/J.CIRP.2019.04.082.

[33] Preston, F., 1927, The theory and design of plate glass polishing machines, Journal of the Society of Glass Technology, 11:214–256.

[34] Hokkirigawa, K., Kato, K., 1988, An experimental and theoretical investigation of ploughing, cutting and wedge formation during abrasive wear, Tribology International, 21/1:51–57, DOI:10.1016/0301-679X(88)90128-4.

[35] Avient, B. W. E., Goddard, J., Wilman, H., 1960, An experimental study of friction and wear during abrasion of metals, Proceedings of the Royal Society of London. Series A. Mathematical and Physical Sciences, 258/1293:159–180, DOI:10.1098/rspa.1960.0180.

[36] Samuels, L. E., Mulhearn, T. O., 1962, The abrasion of metals:, 5:478–498.

[37] Kayaba, T., Hokkirigawa, K., Kato, K., 1986, Analysis of the abrasive wear mechanism by successive observations of wear processes in a scanning electron microscope, Wear, 110/3–4:419–430, DOI:10.1016/0043-1648(86)90115-8.

[38] Hashimoto, F., Yamaguchi, H., Krajnik, P., Wegener, K., Chaudhari, R., et al., 2016, Abrasive fine-finishing technology, CIRP Annals - Manufacturing Technology, 65/2:597–620, DOI:10.1016/j.cirp.2016.06.003.

[39] Hilerio, I., Mathia, T., 2009, Interface mass transfer during the tribofinishing process, Journal of Materials Processing Technology, 209/20:6057–6061, DOI:10.1016/j.jmatprotec.2009.08.012.

[40] Lade, P. V., Nelson, R. B., 1987, Modelling the elastic behaviour of granular materials, International Journal for Numerical and Analytical Methods in Geomechanics, 11/5:521–542, DOI:10.1002/nag.1610110507.

[41] M.Das, B., 2008, Advanced soil mechanics, Taylor & F. London and New York: Taylor & Francis.

[42] 2017, Extended Drucker-Prager models. [Online]. Available: https://abaqus-docs.mit.edu/2017/English/SIMACAEMATRefMap/simamat-c-druckerprager.htm. [Accessed: 21-Dec-2020].

[43] Benker, H., 2000, Constitutive Modelling of Granular Materials. Springer-Verlag Berlin Heidelberg GmbH.

[44] Dano, C., Hicher, P.-Y., Tailliez, S., Varjabédian, M., 2002, Identification des paramètres de comportement des sols injectés par analyse inverse d'essais pressiométriques, Revue française de génie civil, 6/4:631–660, DOI:10.3166/rfgc.6.631-660.

[45] Schanz, T., Vermeer, P. A., 1996, Angles of friction and dilatancy of sand, Geotechnique, 46/1:145–151, DOI:10.1680/geot.1996.46.1.145.

[46] Grange, F., 2014, PhD thesis: Étude expérimentale et numérique du polissage par tribofinition de l'alliage de titane Ti17, École Centrale de Lyon.

[47] Youd, T. L., 1972, Factors Controlling Maximum and Minimum Densities of Sands., ASTM Special Technical Publication, /October:98–112, DOI:10.1520/STP37866S.

[48] Angelim, R. R., Cunha, R. P., Sales, M. M., Determining the Elastic Deformation Modulus From a Compacted Earth Embankment Via Laboratory and Ménard Pressuremeter Tests.

[49] Ghafghazi, M., 2005, Accurate Determination of the Critical State Friction Angle From Triaxial Tests, /September 2005.

[50] Bolton, M. D., 1986, The strength and dilatancy of sands, Geotechnique, 36/1:65–78, DOI:10.1680/geot.1986.36.1.65.

[51] Vermeer, P. A., de Borst, R., 1984, Non-Associated Plasticity for Soils, Concrete and Rock., Heron, 29/3:1–64.

[52] Hashimoto, Y., Ito, T., Nakayama, Y., Furumoto, T., Hosokawa, A., 2021, Fundamental investigation of gyro finishing experimental investigation of contact force between cylindrical workpiece and abrasive media under dry condition, Precision Engineering, 67:123–136, DOI:10.1016/j.precisioneng.2020.09.009.

[53] Saljé, O. E., Paulmann, R., 1988, Relations Between Abrasive Processes, CIRP Annals - Manufacturing Technology, 37/2:641–648, DOI:10.1016/S0007-8506(07)60761-6.

[54] Shaw, M. C., 1996, Principles of abrasive processing. .

[55] Yingjie, L., Xingui, B., Keqiang, C., 1985, A study on the formation of wear debris during abrasion, Tribology International, 18/2:107–111, DOI:10.1016/0301-679X(85)90047-7.

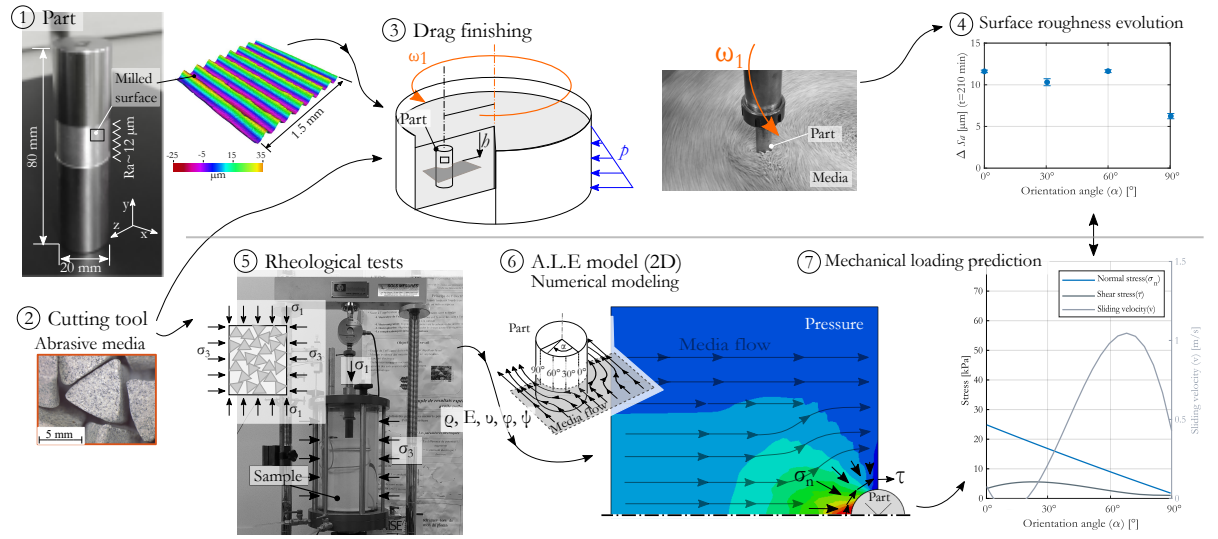
1 Part
Milled surface
Ra~12 µm
80 mm
20 mm
1.5 mm
-25 -5 15 35
µm
3 Drag finishing
ω1
Part
p
ω1
Part
Media
4 Surface roughness evolution
Δ Sa [µm] (t=210 min)
Orientation angle ⟨α⟩ [°]
2 Cutting tool
Abrasive media
5 mm
5 Rheological tests
σ1
σ2
σ3
Sample
6 A.L.E model (2D)
Numerical modeling
Part
90° 60° 30° 0°
Media flow
ϱ, E, υ, φ, ψ
Pressure
Media flow
σn
τ
Part
7 Mechanical loading prediction
Normal stress(σn)
Shear stress(τ)
Sliding velocity(v)
Stress [kPa]
Sliding velocity (v) [m/s]
Orientation angle ⟨α⟩ [°]